Available online at www.sciencedirect.com

ScienceDirect

Advances in Space Research 73 (2024) 3515–3535

ADVANCES IN SPACE RESEARCH (a COSPAR publication)

www.elsevier.com/locate/asr

Anisotropic ionospheric scintillation in weak scattering regime

Dmytro Vasylyev [a,*], Yannick Béniguel [b], Volker Wilken [a], Martin Kriegel [a] Jens Berdermann [a]

[a] Institute for Solar-Terrestrial Physics, German Aerospace Center, Kalkhorstweg 53, Neustrelitz 17235, Germany
[b] Informatique Electromagnétisme Electronique Analyse Numérique (IEEA), Promenade Paul Doumer 13, Courbevoie/Paris 92400, France

Received 24 March 2023; received in revised form 17 August 2023; accepted 8 September 2023
Available online 15 September 2023

Abstract

Transionospheric radio signals might undergo random modulations of their amplitude and phase caused by scattering on irregular structures in the ionosphere. These scintillation phenomena are highly anisotropic, depend on local geomagnetic field configuaration and on the relative position of the signal receiver and scattering irregularity. We derive analytical expressions of anisotropic amplitude and phase scintillation indices using the model of a thin random phase screen. These results extend the classical derivations of [C. Rino, Radio Sci. **14**, 1135 (1979)] to a larger domain of applicability including very slant propagation links of the radio wave signals. The derived generalization is based on the assumption that the ionospheric scattering layer has a spherical symmetry as opposed to the original Rino's assumption of a plan-parallel ionospheric layer. The derived scintillation indices have the simpler analytical form, determine the regions of enhanced scintillation by taking into account the finite curvature of the Earth and of the ionospheric shell, and are divergence-free for large zenith angles of propagation links. For the illustration we discuss the geometric enhancement of scintillation for communication links via a geostationary beacon satellite over the equator.

Keywords: Ionospheric scintillation; Random phase screen method; Anisotropic medium; Scintillation indices; Weak scattering

1. Introduction

Electron density irregularities in the nighttime ionosphere are responsible for causing amplitude and phase scintillation of transionospherically propagating radio waves. Such irregularities are usually aligned along the geomagnetic field lines of force, are elongated along these lines, and show complex morphology. Due to these features of ionospheric inhomogeneities, the resulting scintillation indices are anisotropic, i.e., the fluctuation levels of the transmitted radio wave depend on the receiver zenith and azimuth angles of the transionospheric link as well as on the anisotropy parameters (Kumagai and Ogawa, 1986; Gola et al., 1992; Anderson and Straus, 2005; Afraimovich et al., 2011; Jandieri et al., 2017; Bezler et al., 2019; Hong et al., 2020; Yang and Morton, 2020).

Several models of anisotropic random ionospheric medium have been proposed in multiple studies (Briggs and Parkin, 1963; Singleton, 1970; Mikkelsen et al., 1978). The usual approach is to restrict own attention on the second-order statistical correlation properties of the electron density fluctuations of ionospheric irregularities. For anisotropic medium the value of correlation radius would depend on the direction of the vector that connects two spatial points at which the correlation properties of electron density fluctuations are studied. For example, the correlation radius for a field-aligned anisotropic irregularity is

* Corresponding author.
E-mail addresses: dmytro.vasylyev@dlr.de (D. Vasylyev), beniguel@ieea.fr (Y. Béniguel), volker.wilken@dlr.de (V. Wilken), martin.kriegel@dlr.de (M. Kriegel), jens.berdermann@dlr.de (J. Berdermann).

https://doi.org/10.1016/j.asr.2023.09.021
0273-1177/© 2023 COSPAR. Published by Elsevier B.V.

larger in the direction of the geomagnetic field when comparing to any other direction. For analytic calculations, surfaces where the correlation radius is set to be constant are usually approximated by ellipsoids. Such model is well justified in the spaced-receiver correlation experiments of diffraction pattern of transionospheric signals (Briggs et al., 1950; Costa et al., 1988).

Based on the ellipsoidal model for anisotropic electron density fluctuations, C. Rino in (Rino, 1979a) managed to obtain the analytic formulas for the scintillation indices of the electromagnetic wave scattered on such inhomogeneities. This model is applicable for a weak scattering regime, when the irregular ionosphere can be considered as a thin random phase-changing screen with the prescribed statistical properties. The Rino approach became later the cornerstone in the development of the global climatological scintillation model WBMOD (Secan and Fremouw, 1983; Secan et al., 1995; Secan et al., 1997), which has been validated in multiple studies (Knight et al., 1999; Cervera et al., 2001; Forte and Radicella, 2005; Priyadarshi and Wernik, 2013; Carter et al., 2014). The Rino model remains a popular tool in studies of different aspects of ionospheric scintillation (Wernik et al., 2007; Rino, 2011; Carrano et al., 2012a; Carrano et al., 2012b; Deshpande et al., 2014). This can be attributed to the fact that the model provides the closed analytical expressions for the scintillation indices, uses plausible assumptions, and is applicable in multiple practical situations.

One of the premises of this theoretical treatment is the assumption that the source of the radio signal is positioned in near vertical direction to the ground-based receiver. In this approximation the effects connected to the finite curvature of the ionospheric layer can be neglected, while the slant signal propagation paths are treated via the series of appropriate projection transformations. As an example of such transformations, the vertical distances are projected to the slant ones via the multiplication by the mapping function $\sec\theta$, where θ is the observer zenith angle. It is clear that the secant function diverges at the zenith angles close to $\pi/2$ radians and therefore yields the inadequate values for the slant ranges at these angles. In fact, the inclusion of effects connected with the finite curvature of the Earth and of the ionospheric layer is necessary for the very slant links.

To our knowledge the first attempt to include the corrections to the classical theory of Rino (1979a,b), aiming to extend its applicability domain to the case of very slant propagation paths, has been undertaken by Priyadarshi and Wernik (2013). Priyadarshi and Wernik performed the qualitative analysis of scintillation indices and treated their divergency for slant links by expressing the satellite elevation angle in terms of the elevation angle of the observer (El-Arini et al., 1994). Still, the functional dependence of the scintillation indices on the elevation angle in this work has been adapted from the original flat-geometry formulation (Rino, 1979a) and thus the proposed modification is not a fully consistent generalization to the spherical geometry. In Vasylyev et al. (2022) we considered the geometric aspects of the scintillation modeling in more consecutive manner and listed the expressions for the scintillation indices in the weak scattering regime assuming the sphericity of the ionospheric shell. The present article provides more details on this treatment of the radio wave propagation in a weakly scattering random medium with the inclusion of spherical geometry of the ionospheric layer and of the Earth surface.

The article is structured as follows. In Section 2 the problem of electromagnetic wave propagation in the random ionosphere is outlined. In Section 3 we derive analytic expressions for scintillation indices taking into account anisotropic effects and considering spherical symmetry of the ionospheric shell and Earth surface. The obtained results are then compared with the Rino model, which utilizes the flat-geometry approximation. In Section 4 the geometric enhancement of scintillation is demonstrated for the vertical and slant signal propagation links. Finally, some concluding remarks are summarized in Section 5.

2. Theory of scintillation: a thin phase screen approach

In this section we summarize the main results of wave propagation theory in a randomly inhomogeneous ionosphere with the emphasis on the thin random phase screen approach. Later on this approach would be used for obtaining the analytical expressions for the anisotropic scintillation indices.

2.1. Wave propagation in a randomly inhomogeneous ionosphere

Let us consider the situation when a sender, placed e.g. on an orbiting or stationary satellite, transmits a signal at some radio frequency band to a ground-based receiver. The signal transverses the layer of the ionosphere. The latter has a randomly inhomogeneous structure under disturbed ionospheric conditions. In this case the slow varying component of the electromagnetic field, $u(\mathbf{r})$, satisfies the following paraxial wave equation (Yeh and Liu, 1982; Tatarski, 2016)

$$2ik\frac{\partial u(\mathbf{r})}{\partial z} + \Delta_\perp u(\mathbf{r}) + 2k^2\delta n(\mathbf{r})u(\mathbf{r}) = 0, \tag{1}$$

where the z axis is chosen along the propagation direction, $\Delta_\perp$ is the Laplace operator component transversal to this direction, k is the wavenumber in the medium, and

$$\delta n(\mathbf{r}) \approx -\frac{r_e\lambda^2}{2\pi}\delta N_e(\mathbf{r}), \tag{2}$$

is the random part of the medium refractive index. Here $r_e \approx 2.818 \times 10^{-15}$ m is the classical electron radius and $\lambda = 2\pi/k$ is the wavelength of the electromagnetic wave, and δN_e is the random component of the ionospheric electron density. It is worth to note that the relationship (2) is approximative and is justified if the wave frequency is

much larger than the plasma frequency (i.e., larger than 1–1.5 MHz).

The Eq. (1) establishes the relationship between the wave function u and the random function δn. In the view of stochastic nature of the function $u(\mathbf{r})$, the properties of the transmitted wave are characterized by the moments of u or by their combinations. One such a combination that is widely used is the intensity or amplitude scintillation index

$$S_4 = \sqrt{\langle I^2 \rangle - \left\langle \frac{I}{\langle I \rangle}^2 \right.}, \tag{3}$$

where $I = |u|^2$ is the intensity of the transmitted wave. The index S_4, as seen from its definition, characterizes the strength of intensity deviations from the mean intensity.

The amplitude scintillation index as defined in Eq. (3) uses the absolute values of the electric field. However, in some applications the information on the strength of phase fluctuations is of higher interest. Denoting the phase departure of the wave detected by the observer as S the index

$$\sigma_S = \sqrt{\langle S^2 \rangle - \langle S \rangle^2} \tag{4}$$

characterizes the strength of phase fluctuations from the mean phase value. Since the phase is a circular variable, this definition is applicable as statistical measure if the phase deviations from the mean are much less than the value of π.

2.2. Thin phase screen approximation

One method for solving Eq. (1) is based on the assumption that the irregular medium is thin enough and the diffraction-associated spreading of the wave propagating within this medium is therefore negligible. This requirement is met if the corresponding r.m.s. angle of scattering is negligibly small, i.e., $(kl_0)^{-1} \ll 1$, with l_0 being the typical scale size of ionospheric irregularities contributing to the diffraction-associated scattering [inner-scale parameter in (Yeh and Liu, 1982)]. In this case we can neglect the term $\Delta_\perp u$ in (1), cf. (Uscinski, 1977), and solve the resulting equation taking the plane wave of the constant amplitude U_0 to be the associated boundary condition. The solution for this part of propagation in the medium reads as

$$u_0(\mathbf{r}_\perp) = U_0 e^{i\,\delta\varphi(\mathbf{r}_\perp)}, \tag{5}$$

where $\mathbf{r}_\perp = (x \quad y)^T$ is the transverse component of position vector $\mathbf{r}$ and

$$\delta\varphi(\mathbf{r}_\perp) = k \int_0^s \delta n(\mathbf{r}) \mathrm{d}z = -r_e \lambda \int_0^s \delta N_e(\mathbf{r}) \mathrm{d}z \tag{6}$$

is the phase increment gained while propagating through a thin slab of the random medium. In general, the integration in Eq. (6) is performed along the slant path with the length s corresponding to the distance from the screen and the receiver defined in Eq. (A.15) of Appendix A or in Eq. (C.8) of Appendix C. We also note that since the ionosphere has a finite thickness and δN_e is zero at some distance Δs, the limits of integration in Eq. (6) can be restricted to the interval $[0, \Delta s]$.

Beyond the phase screen, the random component δn in Eq. (1) is negligible and the diffraction effects associated with the term $\Delta_\perp u$ become important. Thus, one can consider Eq. (5) as the boundary condition of the parabolic Eq. (1) with the omitted random term. This corresponds to the approximation of a thin random phase-changing screen (Booker et al., 1950; Hewish, 1951; Briggs and Parkin, 1963; Rino, 1979a), which yields the following expression for the field at distance s from the phase screen (Wernik et al., 1983):

$$u(\mathbf{r}_\perp, s) = U_0 \exp\left[\chi(\mathbf{r}_\perp, s) - iS(\mathbf{r}_\perp, s)\right], \tag{7}$$

$$\chi(\mathbf{r}_\perp, z) = \frac{k}{2\pi z} \int \delta\varphi(\mathbf{r}'_\perp) \cos\left(\frac{k}{2z}|\mathbf{r}_\perp - \mathbf{r}'_\perp|^2\right) \mathrm{d}^2\mathbf{r}'_\perp, \tag{8}$$

$$S(\mathbf{r}_\perp, z) = \frac{k}{2\pi z} \int \delta\varphi(\mathbf{r}'_\perp) \sin\left(\frac{k}{2z}|\mathbf{r}_\perp - \mathbf{r}'_\perp|^2\right) \mathrm{d}^2\mathbf{r}'_\perp, \tag{9}$$

where $\chi(\mathbf{r}) = \log(|u(\mathbf{r})|/U_0)$ is the log-amplitude of the wave and S is its phase departure.

2.3. Statistical characterization in the medium

We are interested in derivation of the scintillation indices (3) and (4), which are related to correlation functions of quantities (8), (9). For this purpose we define the correlation function as

$$\begin{aligned}\rho_X(\mathbf{r}_1, \mathbf{r}_2) =& \langle [X(\mathbf{r}_1) - \langle X(\mathbf{r}_1) \rangle][X(\mathbf{r}_2) - \langle X(\mathbf{r}_2) \rangle] \rangle \\ \equiv& \langle X(\mathbf{r}_1) X(\mathbf{r}_2) \rangle,\end{aligned} \tag{10}$$

where X is the wave log-amplitude χ or the phase shift S. Here we have used $\langle \chi \rangle = \langle S \rangle = 0$ as the consequence of assumption that the random phase of the phase screen is detrended, i.e. $\langle \delta\varphi \rangle = 0$. For spatially homogeneous propagation media the correlation function can be written as $\rho_X(\mathbf{r}_1, \mathbf{r}_2) = \rho_X(\mathbf{r}_1 - \mathbf{r}_2)$. Using the definition (4) one can then deduce the phase scintillation index from its correlation function (10) as

$$\sigma_S^2 = \rho_S(\mathbf{r}_\perp = 0, s). \tag{11}$$

Here and in the following the subscript S refers to the phase departure from expected value and which is measured at the distance s from the screen. For the weak scattering regime, covered by the thin phase screen model, the intensity scintillation index (3) is expressed in terms of the log-amplitude correlation index as (Clifford and Yura, 1974; Fante, 1975a):

$$S_4^2 = \exp\left[4\rho_\chi(0, s)\right] - 1. \tag{12}$$

For $\rho_\chi(0, s) \ll 1$ this expression reduces to $S_4^2 \approx 4\rho_\chi(0, s)$, the expression used in multiple studies, cf. (Rino, 1979a; Tatarski, 2016). The functional dependence of Eq. (12) is

a manifestation of the log-normal statistics for the wave intensity, often observed under quite ionospheric conditions (Rino et al., 1976; Fremouw et al., 1980).

In order to obtain the required correlation functions $\rho_{\chi,S}$, we first introduce the concept of the power spectral density (PSD). For the spatially homogeneous random field X the PSD, denoted as $\Phi_X(\boldsymbol{\kappa})$, is simply the Fourier image of the correlation function ρ_X. Hence, it is defined in the reciprocal spatial domain of spatial frequencies $\boldsymbol{\kappa} = 2\pi/\mathbf{r}$. In this case, by substituting Eqs. (8) and (9) in (10), one can express the correlation functions of the log-amplitude and phase fluctuations in terms of the PSD of the screens phase increment, $\Phi_{\delta\varphi}$, as (Yeh and Liu, 1982):

$$\rho_\chi(\mathbf{r}_\perp, s) = \int \Phi_{\delta\varphi}(\boldsymbol{\kappa}_\perp) \sin^2\left(\frac{s\kappa_\perp^2}{2k}\right) \cos(\boldsymbol{\kappa}_\perp \cdot \mathbf{r}_\perp) \mathrm{d}^2\boldsymbol{\kappa}_\perp, \tag{13}$$

$$\rho_S(\mathbf{r}_\perp, s) = \int \Phi_{\delta\varphi}(\boldsymbol{\kappa}_\perp) \cos^2\left(\frac{s\kappa_\perp^2}{2k}\right) \cos(\boldsymbol{\kappa}_\perp \cdot \mathbf{r}_\perp) \mathrm{d}^2\boldsymbol{\kappa}_\perp. \tag{14}$$

These expressions determine the correlation functions in the plane transversal to the propagation direction and placed at a distance s from the phase screen. From the operational point of view, the plane, in which correlation analysis is performed, is taken to be the tangent to the Earth surface at the receiver location. Adaptation of Eqs. (13), (14) to such measurement geometry is considered in Appendix B. For our further analysis we would be interested in autocorrelation of values measured in the same spatial point $\mathbf{r}_\perp = 0$, so we can use Eqs. (13), (14) without any additional adjustment to the coordinate system of the receiver.

Since the random phase screen increment $\delta\varphi$ is defined as a model variable, it should be connected to the empirical quantity characterizing the random ionosphere, such as the electron density fluctuation δN_e. We now assume that a region of the random irregular electron density is bounded within the spherical shell with the radii $R_\oplus + h_p$ and $R_\oplus + h_p - \Delta h$, where $R_\oplus$ is the Earth radius, h_p is the altitude of the phase screen, and Δh is the thickness of the shell. We also assume that the random ionospheric medium is spatially homogeneous within this shell. Then, by using the relationship (6) one obtains[1]

$$\Phi_{\delta\varphi}(\boldsymbol{\kappa}_\perp) = 2\pi \Delta s\, \lambda^2 r_e^2 \Phi_{\delta N_e}(\boldsymbol{\kappa}_\perp, 0), \tag{15}$$

where $\Delta s = \Delta h \cdot M$ is the slant thickness of the shell with M being the vertical-to-slant mapping function, which explicit form is derived in Appendix C. The expression (15) relates the two-dimensional model spectrum for phase increment and the three-dimensional spectrum of electron density fluctuations. The latter can be obtained experimentally by means of the correlation analysis of electron density fluctuations and exhibits the power-law dependence on the spatial frequency $\boldsymbol{\kappa}$. Such dependence can be modeled by the von Karman spectrum (von Karman, 1948; Vasylyev et al., 2022)

$$\Phi_{\delta N_e}(\boldsymbol{\kappa}) = \frac{\langle \delta N_e^2 \rangle r_0^3}{\pi^{3/2}} \frac{\Gamma\left(\frac{p+2}{2}\right)}{\Gamma\left(\frac{p-1}{2}\right)} \frac{(r_0\kappa_0)^{p-1}}{\left(Q(\boldsymbol{\kappa}) + r_0^2\kappa_0^2\right)^{\frac{p+2}{2}}} \tag{16}$$

defined in the spatial frequency range $\kappa_0 \ll \kappa \ll \kappa_m$ with κ_0 being associated with the largest spatial scale of random ionospheric inhomogeneities, while κ_m being associated with the inner-scale l_0 of the random ionosphere. Here $\langle \delta N_e^2 \rangle$ is the variance of the electron density fluctuations, r_0 is some conventionally chosen reference correlation radius of the medium, p is the (one-dimensional) spectral index, and $\Gamma(x)$ is the gamma function. The (dimensionless) function $Q(\boldsymbol{\kappa})$ is some quadratic form of the spatial vector $\boldsymbol{\kappa}$ that incorporates the possibility to include anisotropy of random inhomogeneities in consideration. The model parameters $\langle \delta N_e^2 \rangle, \kappa_0, r_0, p$ and anisotropy characteristics can be inferred from the empirical spectra (Dyson et al., 1974; Phelps and Sagalyn, 1976; Kelley et al., 1982; Lay et al., 2018; De Michelis et al., 2021).

3. Derivation of scintillation indices under the spherical geometry assumption

In this section we derive the ionospheric scintillation indices taking into account effects of anisotropy of ionospheric irregularities and by assuming that both the Earth surface and the ionospheric shell have the finite radii of curvature and spherical symmetry. The proposed spherical-geometry model is the elaboration of the original flat-geometry model of (Rino, 1979a), whose results are also summarized at the end of this section for the sake of convenience of referencing and comparison with derived results.

3.1. Anisotropy of ionospheric irregularities

To start with, we consider the model for medium anisotropy. To this end, we derive the quadratic form $Q(\boldsymbol{\kappa})$, that enters the spectrum (16), and relate the coefficients of this form to the physically measurable quantities. As has been mentioned already, the scintillation-causing ionospheric irregularities are primarily anisotropic with tendency to be elongated in the direction of the geomagnetic lines of force (Tereshchenko et al., 1999; Portillo et al., 2008; Mevius et al., 2016; Liu et al., 2021). In order to include this anisotropy in the scintillation theory we assume that the surface of constant correlation of electron density fluctuations can be approximated by the concentric ellipsoidal shapes (Singleton, 1970; Moorcroft and Arima, 1972; Kersley et al., 1988; Bhattacharyya et al., 1992). For the specified radius of correlation, r_0, the equation of ellipsoidal surface of constant correlation can be written as

[1] In order to underline the difference in scattering geometries considered within the spherical- (this article) and flat-geometry (Ref. (Rino and Fremouw, 1977)) approximations, we discuss the corresponding derivations of relationships between $\Phi_{\delta\varphi}$ and $\Phi_{\delta N_e}$ in Appendix D providing some further details.

$$\left(\frac{\Delta \mathtt{t}}{r_0}\right)^2 + \left(\frac{\Delta \mathtt{s}}{\alpha r_0}\right)^2 + \left(\frac{\Delta \mathtt{r}}{\beta r_0}\right)^2 = \text{const.} \tag{17}$$

Here $\Delta\mathtt{t}, \Delta\mathtt{s}, \Delta\mathtt{r}$ are the components of the position difference vector with respect to the so-called Singleton coordinate system $\mathtt{r}, \mathtt{s}, \mathtt{t}$. The latter is defined such that the coordinate center coincides with the center of the correlation ellipsoid and its coordinate axes are aligned along the major semi-axes of the ellipsoid. The $\mathtt{t}$-axis is chosen to be aligned along the minor semi-axis of length r_0 and the $\mathtt{s}$-axis is aligned along the major semi-axis of length αr_0. The remaining $\mathtt{r}$-axis is aligned along the semi-axis of length βr_0. The parameters α, β are the scaling factors characterizing the anisotropy of a particular ionospheric irregularity.

The correlation function of electron density fluctuations, $\rho_{\delta N_e}$, is assumed to depend on the quadratic form defined by Eq. (17). Correspondingly, the power spectral density, $\Phi_{\delta N_e}$, is the function of the similar diagonal quadratics in the reciprocal space $\kappa_\mathtt{r}, \kappa_\mathtt{s}, \kappa_\mathtt{t}$

$$Q(\kappa_\mathtt{t}, \kappa_\mathtt{s}, \kappa_\mathtt{r}) = r_0^2\kappa_\mathtt{t}^2 + (\alpha r_0)^2\kappa_\mathtt{s}^2 + (\beta r_0)^2\kappa_\mathtt{r}^2. \tag{18}$$

On the other hand, the expressions for the correlation and spectral density functions in Section 2.2 have been obtained as the function of coordinates $\mathbf{r}$ and $\boldsymbol{\kappa}$ associated with the wave propagation geometry, e.g., the z-axis has been chosen to be aligned with the wave vector $\boldsymbol{k}$ of the propagating radio wave. In order to incorporate the anisotropy effects, we thus need to perform a series of transformations of the ellipsoid defined in the Singleton coordinates for redefining it in terms of the position difference variable components. The position difference variables, in turn, are defined in the conventional coordinate system x, y, z.

In order to perform the required coordinate transformation, we follow the procedure given in Rino and Fremouw (1977, 1979a). For definiteness we consider the transformation in the spatial domain, i.e., for the moment we focus our attention on rotations of the correlation ellipsoid. For that we express Eq. (17) in terms of the conventional coordinate system, i.e., in terms of the position difference components $\Delta x, \Delta y, \Delta z$. This procedure involves the transformation from the conventional coordinates associated with the propagation geometry to the local coordinate system, e.g., the North-East-Down (NED) coordinate system with the origin at the center of the correlation ellipsoid. This is accomplished by the consequent transformation from the NED coordinates to the Singleton ones. The last step is called the Singleton transformation and can be written using the notation n, e, d for the NED coordinates as

$$\begin{pmatrix} \Delta\mathtt{s} \\ \Delta\mathtt{r} \\ \Delta\mathtt{t} \end{pmatrix} = R_x(\gamma)R_y(\psi)R_z(\delta)\begin{pmatrix} \Delta n \\ \Delta e \\ \Delta d \end{pmatrix}, \tag{19}$$

where δ is the magnetic dip angle, ψ is the magnetic declination angle, and γ is the tilt angle of the magnetic field lines. The rotation matrices

$$R_x(\xi) = \begin{pmatrix} 1 & 0 & 0 \\ 0 & \cos\xi & -\sin\xi \\ 0 & \sin\xi & \cos\xi \end{pmatrix},$$

$$R_y(\xi) = \begin{pmatrix} \cos\xi & 0 & \sin\xi \\ 0 & 1 & 0 \\ -\sin\xi & 0 & \cos\xi \end{pmatrix},$$

$$R_z(\xi) = \begin{pmatrix} \cos\xi & -\sin\xi & 0 \\ \sin\xi & \cos\xi & 0 \\ 0 & 0 & 1 \end{pmatrix}$$

perform the rotations on an angle ξ with respect to the corresponding x, y or z axis. The geometrical meaning of rotational transformations in Eq. (19) can be inferred from Fig. 1.

The transformation of the components of the position difference vector, defined in the conventional coordinates to the components in the NED-coordinate system, is

$$\begin{pmatrix} \Delta n \\ \Delta e \\ \Delta d \end{pmatrix} = R_z(-\phi_p)R_y(\theta_p)\begin{pmatrix} \Delta x \\ \Delta y \\ \Delta z \end{pmatrix}, \tag{20}$$

where ϕ_p and θ_p are the azimuth and nadir (zenith) angles of the wave propagation path at the location of the ionospheric scattering point, see also Fig. 2. The relationships between the local coordinates ϕ_p, θ_p and the coordinates of the sender and the receiver are summarized in Appendix A. The combination of Eqs. (19) and (20) yields the required transformation from the conventional coordinates x, y, z to the Singleton coordinates $\mathtt{r}, \mathtt{s}, \mathtt{t}$. The diagonal quadratic form (17) is expressed in terms of the NED coordinates as

$$q(\Delta n, \Delta e, \Delta d) = (\Delta n \quad \Delta e \quad \Delta d) \cdot C \begin{pmatrix} \Delta n \\ \Delta e \\ \Delta d \end{pmatrix}, \tag{21}$$

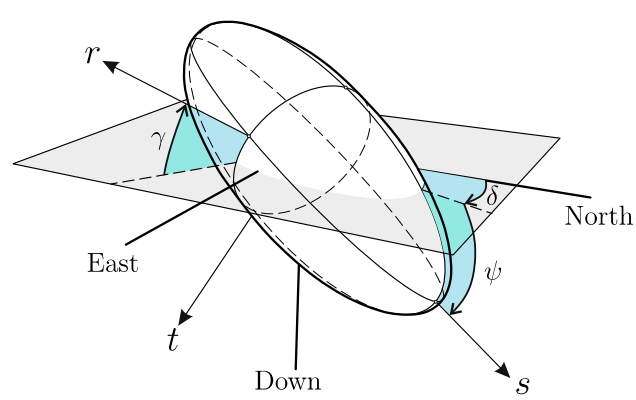

Fig. 1. Orientation of the ellipsoid of constant correlation in the North-East-Down (NED) local coordinate system. The principal axes of the ellipsoid are aligned along the Singleton coordinate axes $\mathtt{s}, \mathtt{r}, \mathtt{t}$ and are rotated with respect to the NED coordinates on the magnetic declination, δ, magnetic inclination (dip), ψ, and tilt, γ, angles.

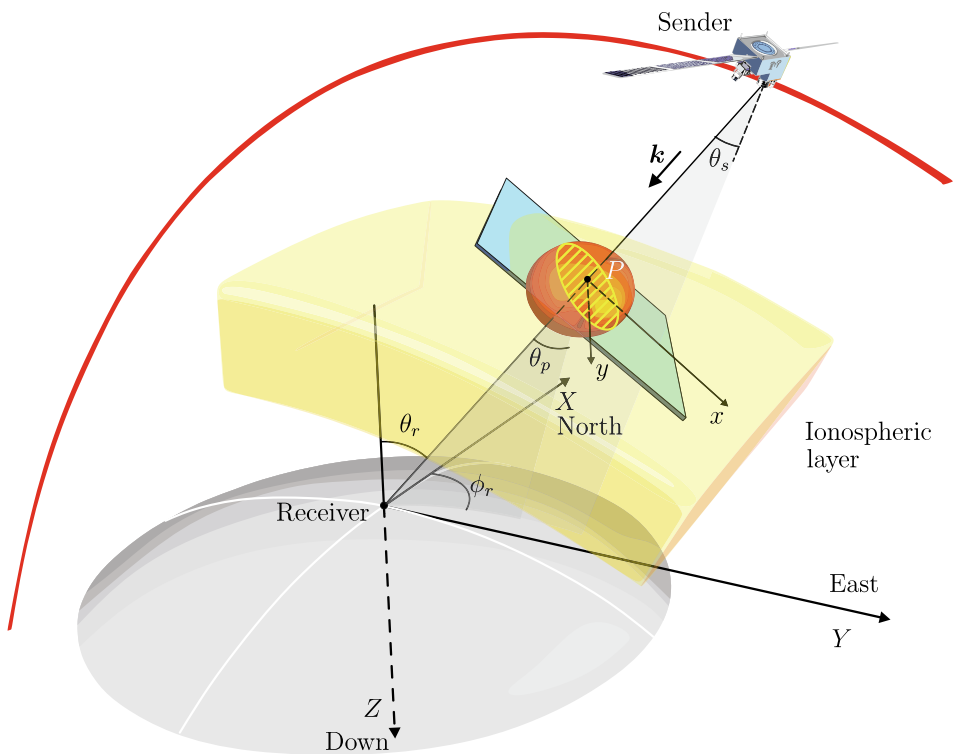

Fig. 2. Scattering geometry for the signal that propagates in the disturbed ionosphere. The relative position of the sender, receiver and the scattering point P defines the plane of the phase screen which is transversal to the wave vector of the signal wave. This plane crosses the correlation ellipsoid and forms the elliptic cross-section (hatched area). Some used coordinate systems are indicated along with the zenith (nadir) angles $\theta_r, \theta_p, \theta_s$ and the receiver azimuth angle ϕ_r.

$$C = \left[D^{-1}R_x(\gamma)R_y(\psi)R_z(\delta)\right]^T D^{-1}R_x(\gamma)R_y(\psi)R_z(\delta).$$

Here

$$D = r_0\begin{pmatrix} \alpha & 0 & 0 \\ 0 & \beta & 0 \\ 0 & 0 & 1 \end{pmatrix} \tag{22}$$

is the scaling matrix that deforms isotropic correlation surface, i.e., the sphere of unit radius, into the required ellipsoidal surface. The elements of the matrix C are calculated as

$$\begin{aligned}
C_{11} = {} & \tfrac{1}{r_0^2}[\alpha^{-2}\cos^2\psi\cos^2\delta \\
& + \sin^2\psi\cos^2\delta\left(\cos^2\gamma + \beta^{-2}\sin^2\gamma\right) \\
& + \sin^2\delta\left(\sin^2\gamma + \beta^{-2}\cos^2\gamma\right) \\
& + \tfrac{1}{2}\sin 2\gamma\sin\psi\sin 2\delta\left(\beta^{-2}-1\right)], \\
C_{22} = {} & \tfrac{1}{r_0^2}\left[\alpha^{-2}\cos^2\psi\sin^2\delta\right. \\
& + \sin^2\psi\sin^2\delta\left(\cos^2\gamma + \beta^{-2}\sin^2\gamma\right) \\
& + \cos^2\delta\left(\sin^2\gamma + \beta^{-2}\cos^2\gamma\right) \\
& - \tfrac{1}{2}\sin 2\gamma\sin\psi\sin 2\delta\left(\beta^{-2}-1\right)], \\
(23)C_{33} = {} & \tfrac{1}{r_0^2}\left[\alpha^{-2}\sin^2\psi + \cos^2\psi\left(\cos^2\gamma + \beta^{-2}\sin^2\gamma\right)\right],
\end{aligned}$$

$$\begin{aligned}
C_{12} = C_{21} = {} & \frac{1}{2r_0^2}\sin 2\delta\left[\sin^2\gamma + \beta^{-2}\cos^2\gamma\right. \\
& \left.-\alpha^{-2}\cos^2\psi - \sin^2\psi\left(\cos^2\gamma + \beta^{-2}\sin^2\gamma\right)\right] \\
& + \frac{r_0^2}{2}\cos 2\delta\sin 2\gamma\sin\psi\left(\beta^{-2}-1\right), \\
C_{13} = C_{31} = {} & \frac{1}{2r_0^2}\sin 2\psi\cos\delta\left(\alpha^{-2} - \cos^2\gamma - \beta^{-2}\sin^2\gamma\right) \\
& - \frac{1}{2r_0^2}\sin 2\gamma\cos\psi\sin\delta\left(\beta^{-2}-1\right), \\
C_{23} = C_{32} = {} & -\frac{1}{2r_0^2}\sin 2\psi\sin\delta\left(\alpha^{-2} - \cos^2\gamma - \beta^{-2}\sin^2\gamma\right) \\
& - \frac{1}{2r_0^2}\sin 2\gamma\cos\psi\cos\delta\left(\beta^{-2}-1\right).
\end{aligned} \tag{23}$$

The particular case of zero magnetic declination, $\delta = 0$, has been considered by Rino and Fremouw (1977).

In order to express the quadratic form (17) in terms of the x, y, z coordinates, one needs to perform the final transformation according to Eq. (20). For the sake of convenience we switch to the similar quadratic form (18) defined in the reciprocal space. It can be expressed in terms of the spatial frequency vector $\boldsymbol{\kappa}$, reciprocal to the argument $\mathbf{r}_1 - \mathbf{r}_2 = (\Delta x \quad \Delta y \quad \Delta z)^T$ of the autocorrelation function (10), as

$$Q(\boldsymbol{\kappa}) = \left[R_z(-\phi_p)R_y(\theta_p)\boldsymbol{\kappa}\right]^T \cdot \overline{C}R_z(-\phi_p)R_y(\theta_p)\boldsymbol{\kappa}, \tag{24}$$

where the matrix $\overline{C}$ is obtained from the matrix C, by performing the replacement: $r_0 \to 1/r_0, \alpha \to 1/\alpha, \beta \to 1/\beta$ in Eq. (23). The calculation of the quadratic form (24) can be simplified by noting that the calculation of scintillation indices requires the knowledge of the quadratic form $Q(\boldsymbol{\kappa}_\perp, 0)$, where the spatial vector component along the propagation direction is set to zero, see Eq. (15). This simplification yields

$$Q(\boldsymbol{\kappa}_\perp, 0) = \mathscr{A}\kappa_x^2 + 2\mathscr{B}\kappa_x\kappa_y + \mathscr{C}\kappa_y^2, \tag{25}$$

where

$$\begin{aligned} \mathscr{A} = & \ \overline{C}_{11}\cos^2\theta_p\cos^2\phi_p + \overline{C}_{22}\cos^2\theta_p\sin^2\phi_p \\ + & \ \overline{C}_{33}\sin^2\theta_p - \overline{C}_{12}\cos^2\theta_p\sin 2\phi_p \\ - & \ \overline{C}_{13}\sin 2\theta_p\cos\phi_p + \overline{C}_{23}\sin 2\theta_p\sin\phi_p, \\ \mathscr{B} = & \ \tfrac{1}{2}\left(\overline{C}_{11} - \overline{C}_{22}\right)\cos\theta_p\sin 2\phi_p \\ & + \ \overline{C}_{12}\cos\theta_p\cos 2\phi_p - \overline{C}_{13}\sin\theta_p\sin\phi_p \\ & - \ \overline{C}_{23}\sin\theta_p\cos\phi_p, \\ \mathscr{C} = & \ \overline{C}_{11}\sin^2\phi_p + \overline{C}_{22}\cos^2\phi_p + \overline{C}_{12}\sin 2\phi_p. \end{aligned} \tag{26}$$

The quadratic form (25) corresponds to the elliptical cross-section of the ellipsoid (18) with the plane of the phase screen.

Incorporating formula (25) in the von Karman spectrum (16) one obtains for the properly normalized spectrum the following expression:

$$\Phi_{\delta N_e}(\boldsymbol{\kappa}_\perp, 0) = \alpha\beta r_0^3 C_s \times \frac{r_0^{p-1}}{\left(\mathscr{A}\kappa_x^2 + 2\mathscr{B}\kappa_x\kappa_y + \mathscr{C}\kappa_y^2 + r_0^2\kappa_0^2\right)^{\frac{p+2}{2}}}. \tag{27}$$

Here

$$C_s = \frac{\langle \delta N_e^2 \rangle}{\pi^{\frac{3}{2}}} \frac{\Gamma\left(\frac{p+2}{2}\right)}{\Gamma\left(\frac{p-1}{2}\right)} \kappa_0^{p-1} \tag{28}$$

is the so-called structure parameter. This particular type of spectrum would be used in the following.

3.2. Anisotropic scintillation indices

The spectral model (27) can now be used for calculations of the anisotropic scintillation indices. To this end, one can substitute the power spectral density of the electron density fluctuations (27) in Eq. (15). The latter equation is then used in Eqs. (13) and (14) for calculation of the log-amplitude and phase correlation functions. The resulting integrals can be simplified by making certain observations as discussed below.

If we define the spatial frequency associated with the radius of the first Fresnel zone as $\kappa_f = 2\pi/\sqrt{\lambda s}$, it is reasonable to consider separately the spatial frequency ranges: $\kappa_\perp < \kappa_f$ and $\kappa_\perp > \kappa_f$. A particular spatial frequency $\kappa_\perp$ is inversely proportional to the scale of the associated irregularity if this scale is measured along the direction perpendicular to the propagation direction. In the case of $\kappa_\perp < \kappa_f$, the inhomogeneities are large enough to bend the propagating signal ray. Such refraction scintillation primarily contributes to the random excursion of the phase (Conroy et al., 2022). The amplitude scintillation is negligibly small as the propagation factor $\sin^2\left(s\kappa_\perp^2/2k\right)$ in the integral (13) tends to zero. For the phase fluctuations the corresponding propagation factor $\cos^2\left(s\kappa_\perp^2/2k\right) \approx 1$, and, therefore, the phase scintillation index is primarily associated with the refractive effects. The phase scintillation index can be written then as

$$\sigma_S^2 = \rho_S(0,s) \approx 2\pi\alpha\beta\lambda^2 r_e^2 C_s \Delta s r_0^3 \times \int_{\mathbb{R}^2} \frac{r_0^{p-1}\mathrm{d}^2\boldsymbol{\kappa}_\perp}{\left(\mathscr{A}\kappa_x^2 + 2\mathscr{B}\kappa_x\kappa_y + \mathscr{C}\kappa_y^2 + r_0^2\kappa_0^2\right)^{\frac{p+2}{2}}}. \tag{29}$$

This equation is obtained by substituting Eq. (27) in (15) and then by inserting the resulting spectrum in Eq. (14).

In the second case of $\kappa_\perp > \kappa_f$, the propagation factor in Eq. (13) is finite and shows the oscillating behavior. We can however make the reasonable approximation $\kappa_0 \ll \kappa_f$, i.e., we assume that the transversal scales of the scintillation associated irregularities are smaller than the largest spatial scale of ionospheric inhomogeneities. Such small-scale irregularities contribute merely to the random diffraction of the transmitted electromagnetic waves giving rise primarily to the amplitude scintillation. Additionally to this the major contribution is due to the irregularity scales corresponding to the radius of the first Fresnel zone $\sqrt{\lambda s}$. The amplitude scintillation index can be approximated then as

$$S_4^2 \approx \exp\left[8\pi\alpha\beta\lambda^2 r_e^2 C_s \Delta s r_0^3 \times \int_{\mathbb{R}^2} \frac{r_0^{p-1}\sin^2\left(\frac{s\kappa_\perp^2}{2k}\right)}{\left(\mathscr{A}\kappa_x^2 + 2\mathscr{B}\kappa_x\kappa_y + \mathscr{C}\kappa_y^2\right)^{\frac{p+2}{2}}}\mathrm{d}^2\boldsymbol{\kappa}_\perp\right] - 1. \tag{30}$$

Here we have used the condition $\kappa_0 \ll \kappa_f \leqslant 2\pi/r_0$ along with $r_0\kappa_0 \to 0$ while the value of the outer scale wave number remains finite.

The calculation of the integrals in Eqs. (29) and (30) is summarized in Appendix E. Using the resulting expressions (E.5) and (E.12) for the integrals, one obtains the following expressions for scintillation indices:

$$\sigma_S^2 \approx 4\pi^2 C_s \mathscr{G} p^{-1} \Delta s \lambda^2 r_e^2 \kappa_0^{-p} \tag{31}$$

$$\begin{aligned} S_4^2 \approx & \ \exp\left[8\pi^{\frac{5}{2}} C_s \mathscr{G} \tfrac{1}{p} \tfrac{\Gamma\left(1-\frac{p}{4}\right)}{\Gamma\left(\frac{1}{2}+\frac{p}{4}\right)} \Delta s \lambda^2 r_e^2 \left(\tfrac{s r_0^2}{2k}\right)^{\frac{p}{2}}\right. \\ \times & \ \left.\left(\tfrac{1}{\sqrt{\mathscr{A}\mathscr{C}-\mathscr{B}^2}}\right)^{\frac{p}{2}} P_{\frac{p}{2}}\left(\tfrac{\mathscr{A}+\mathscr{C}}{2\sqrt{\mathscr{A}\mathscr{C}-\mathscr{B}^2}}\right)\right] - 1, \end{aligned} \tag{32}$$

where

$$\mathscr{G} = \frac{\alpha\beta r_0^2}{\sqrt{\mathscr{A}\mathscr{C} - \mathscr{B}^2}} \tag{33}$$

is the so-called geometric factor and $P_\alpha(x)$ is the Legendre function of order α.

Rino (1979a) gives[2] the following interpretation of the result (32). The scintillation index S_4^2 is proportional to $C_s\kappa_f^{-p}$, where $\kappa_f = 2\pi/\sqrt{\lambda s}$ is the Fresnel spatial frequency. Comparing this power law dependence with the three-dimensional spectrum for electron density fluctuations (16), one can conclude that the magnitude of S_4 is modulated by the one-dimensional power spectral density of ionospheric irregularities. This spectrum is evaluated at the spatial frequency associated with the radius of the first Fresnel zone for the considered scattering geometry. We also note that both expressions for scintillation indices do not depend on the correlation radius r_0 as one would expect.

3.3. Comparison with the Rino scintillation model

The obtained expressions (31) and (32) can be compared with the seminal results of (Rino, 1979a), which can be written in the following form:

$$\sigma^2_{S,\mathrm{Rino}} \approx 4\pi^2 C_s \mathscr{G}' p^{-1}\,\Delta h \sec\theta\, \lambda^2 r_e^2 \kappa_0^{-p} \tag{34}$$

$$\begin{aligned} S^2_{4,\mathrm{Rino}} \approx \quad & \exp\Big[8\pi^{\frac{5}{2}} C_s \mathscr{G}' \tfrac{1}{p} \tfrac{\Gamma\left(1-\frac{p}{4}\right)}{\Gamma\left(\frac{1}{2}+\frac{p}{4}\right)} \Delta h \sec\theta \\ & \times \quad \lambda^2 r_e^2 \left(\tfrac{h_p \sec\theta\, r_0^2}{2k}\right)^{\frac{p}{2}} \left(\tfrac{1}{\sqrt{\mathscr{A}'\mathscr{C}' - (\mathscr{B}')^2}}\right)^{\frac{p}{2}} \\ & \times P_{\frac{p}{2}}\left(\sec\theta \frac{\mathscr{A}' + \mathscr{C}' - \mathscr{A}' a_1^2 - 2\mathscr{B}' a_1 a_2 - \mathscr{C}' a_2^2}{2\sqrt{\mathscr{A}'\mathscr{C}' - (\mathscr{B}')^2}}\right)\Big] - 1, \end{aligned} \tag{35}$$

where we extended the applicability of the single scattering result for S_4 index according to Eq. (12). We also express the S_4 index in terms of the Legendre function instead of the hypergeometric function as has been originally done in Rino (1979a), see also Appendix E for details. The reason for this the possibility to write Eq. (35) in more compact form that also enables one to separate the geometric and propagation factors in the resulting formula. The geometric term is defined as

$$\mathscr{G}' = \frac{\alpha\beta r_0^2 \sec\theta}{\sqrt{\mathscr{A}'\mathscr{C}' - (\mathscr{B}')^2}}, \tag{36}$$

where the quadratic form coefficients are

$$\begin{aligned} \mathscr{A}' = \quad & \overline{C}_{11} + \overline{C}_{33}\tan^2\theta\cos^2\phi - 2\overline{C}_{13}\tan\theta\cos\phi, \\ \mathscr{B}' = \quad & \overline{C}_{12} + \tfrac{1}{2}\overline{C}_{33}\tan^2\theta\sin 2\phi \\ & \tan\theta\left(\overline{C}_{13}\sin\phi + \overline{C}_{23}\cos\phi\right), \\ \mathscr{C}' = \; & \overline{C}_{22} + \overline{C}_{33}\tan^2\theta\sin^2\phi - 2\overline{C}_{23}\tan\theta\sin\phi. \end{aligned} \tag{37}$$

These coefficients have an another functional dependence as the coefficients in Eq. (B.1) as a consequence of the flat-geometry approximation used in Rino's theory and the difference in how the phase screen plane is positioned in space. Namely Rino's theory defines the phase screen plane to be transversal to the vertical direction of the ground observer, while in the spherical-geometry approximation, developed in this article, it is transversal to the wave vector of the propagating signal wave.

Another consequence of the flat-geometry approximation is the equivalence of the zenith (nadir) and azimuth angles for the sender, the receiver, and the scattering point. Because of this equivalence we have omitted corresponding indices in Eqs. (34)–(37) for the zenith, θ, and the azimuth, ϕ, angles.

We also note that the positioning of the phase screen plane to be perpendicular to the observer vertical direction is optimal for the description of the signal propagation when the sender is at the receivers zenith. For the slant sender-receiver links the correction term $\mathscr{A}' a_1^2 + 2\mathscr{B}' a_1 a_2 + \mathscr{C}' a_2^2$ appears in the argument of the Legendre function in Eq. (35). The arguments of this quadratic form, $a_1 = \sin\theta\cos\phi, a_2 = \sin\theta\sin\phi$, are the projections of the normalized wave vector $\boldsymbol{k}/k$ on the phase screen plane.

4. Geometric enhancement of scintillation

The scintillation indices (31) and (32) [as well as the indices (34) and (35)] depend on the set of parameters that can be deduced from the experimental data. The integrated irregularity strength parameter $C_s\Delta h$ can be retrieved from the GNSS and SAR satellite scintillation measurements (Belcher et al., 2017; Mohanty et al., 2018; Carrano et al., 2019; Helmboldt and Zabotin, 2022; Ji et al., 2022)[3]. This parameter exhibits dependence on the season, time, magnetic latitude, solar activity, etc. Based on the empirical data, the climatological model $C_s\Delta h$ has been developed within the framework of the WBMOD (Fremouw and Larsinger, 1981; Secan and Fremouw, 1983; Fremouw and Secan, 1984; Secan et al., 1987).

The value of the spectral index p depends on the type of instability involved in the formation of ionospheric irregularities responsible for the random scattering of the signal wave. The typical empirical and theoretical values of p are summarized in (Vasylyev et al., 2022).

The anisotropy parameters α and β have a rich morphology. At high latitudes one has observed the rod-like structures ($\alpha \approx 5-10, \beta \approx 1$) that are elongated along the geomagnetic field lines (Rino et al., 1978; Basu et al., 1991; Wang and Morton, 2017; Conroy et al., 2021). Additionally to these structures, the wing- ($\alpha \approx 10-15, \beta \approx 5$)

[2] Note that the spectral index of Rino (1979a), ν, is related to the one-dimensional spectral index of electron density fluctuations, p, as $\nu = (p+1)/2$.

[3] The relationship of the parameter $C_s\Delta h$, with C_s as defined in Eq. (28), to the parameter C_kL of, e.g., (Carrano et al., 2019) is $C_s\Delta h = \frac{1}{(2\pi)^3}\left(\frac{2\pi}{1000}\right)^{p+2}\cdot C_kL$.

and sheet-like ($\alpha \approx \beta \approx 10$) structures might appear near the exit of the polar convection channel (Rino and Owen, 1980; Rino et al., 1983; Conroy et al., 2021). The mid-latitude irregularities are primarily field-aligned of the rod-type, $\alpha \approx 6, \beta \approx 1$, (Moorcroft and Arima, 1972) (Lay et al., 2018), while the Perkin instability might also form the sheet-like structures (MacDougall and Eadie, 2005). Finally, the equatorial irregularities show a high degree of anisotropy. For example, ellipse-like diffraction patterns on the ground formed by these irregularities show their elongation along the magnetic field lines and the axial ratio to reach the value of 60 : 1 (Koster, 1963; Koster, 1972).

In order to demonstrate the impact of these anisotropy factors along with the type of approximation for the link configuration on the geometric enhancement of scintillation, we plot in Fig. 3 the amplitude scintillation index as a function of the receiver zenith angle and the geomagnetic dip angle. The scintillation index is shown for two types of ionospheric irregularities: wing-like ones, plots (a), (c), and the rod-like structures, plots (b), (d). Despite the plots for both types of irregularities look similar, one can observe that in the case when the irregularity is primarily elongated only in one direction (rod-like structure) the enhancement of scintillation is stronger, plots (b), (d), than in the case when the irregularities are highly anisotropic, as it is the case for the wing-like structures, plots (a) and (c).

The upper row of the plots, Figs. 3 (a), (b), corresponds to the flat-geometry approximation and Eq. (35) is used for the calculation of S_4. Correspondingly, the plots (c), (d) from the lower row of Fig. 3 represent the spherical-geometry approximation, cf. Eq. (32). The graphics in the first column of Fig. 3 sketch the geometry of the sender-receiver links crossing the ionospheric irregularities at two limiting values of the receiver zenith angle, namely, for $\theta_r = 0^\circ$, as indicated by the Roman numbers I, III, and for $\theta_r = 90^\circ$, as indicated by II and IV. The shown ellipsoids correspond to the isosurfaces of the constant correlation, cf. Eq. (17). Using these sketches as a visual aid one can interpret the difference in geometric enhancement regions shown in Figs. 3 (a), (b) and in Figs. 3 (c), (d) as follows.

For the vertical propagation links, marked by I and III, the scintillation index attains small values at small magnetic dip angles. In this case the link crosses the correlation ellipsoid along one of its minor semi-axis. The major semi-axis of correlation ellipsoid lies in the plane transversal to the propagation direction, which results into weak side scattering leading to low scintillation levels observed on

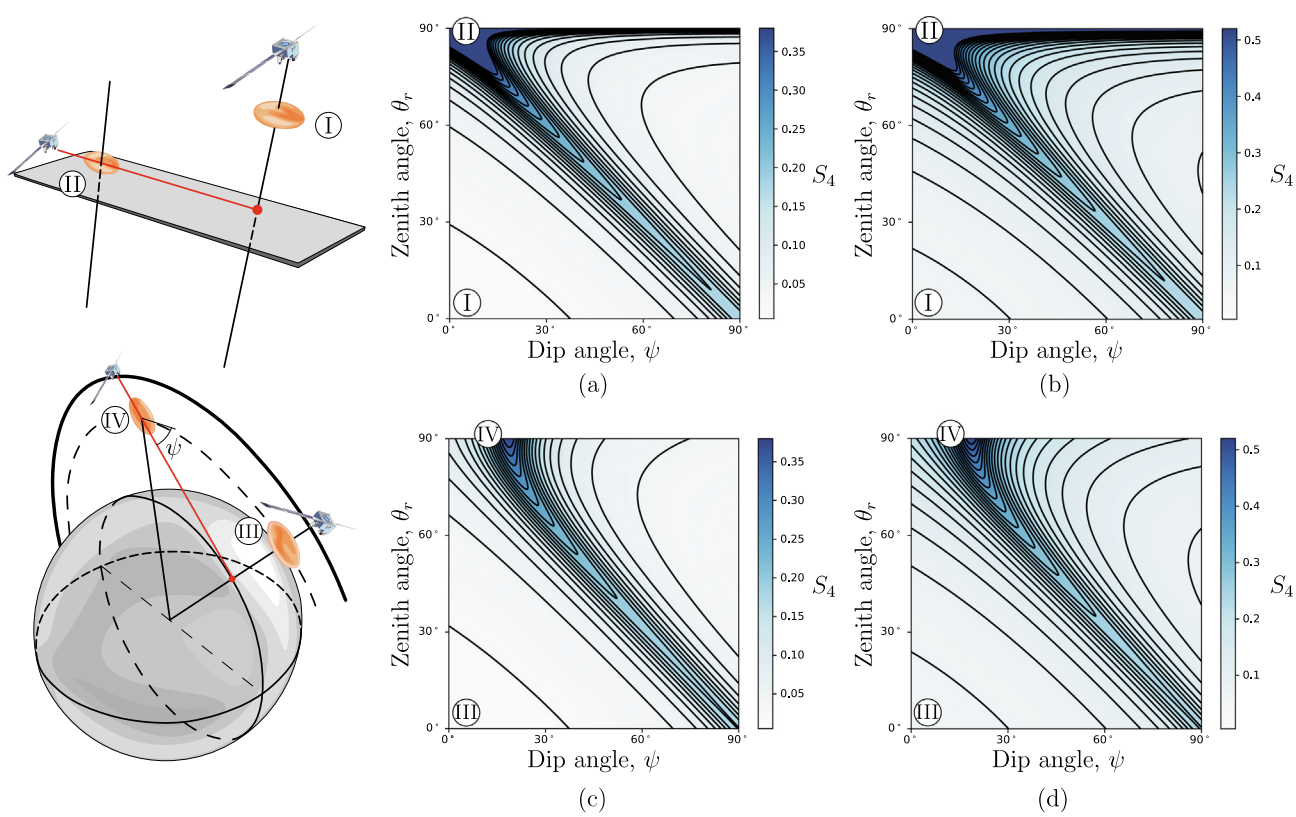

Fig. 3. Enhancement of the amplitude scintillation calculated within the flat-geometry, (a) and (b), and the spherical-geometry, (c) and (d), approximations. Two types of irregularities have been considered in the calculations: wing-like structures with $\alpha = 10, \beta = 5$, figures (a) and (c); rod-like inhomogeneities with $\alpha = 10$ and $\beta = 1$, figures (b) and (d). The Roman numbers indicate regions of values for the receiver zenith angle, θ_r, and for the geomagnetic dip angle, ψ, that correspond to the propagation link configurations sketched on the first column of the figure. The receiver azimuth, magnetic declination, and tilt angles are set to be zero.

the ground. If we change the zenith angle to $\theta_r = 90^\circ$, that corresponds to the cases II and IV, the small values of the dip angle would correspond to the situation when the link crosses the correlation ellipsoids along the major semi-axis. In this case the situation is reversed and the minor semi-axis of the medium correlation ellipsoid lies in the transversal plane. This means that multiple scattering plays an important role and contributes to higher values of scintillation[4]. One can also note the divergent character of indices obtained within the flat-geometry approximation at $\theta_r = 90^\circ$. This is because the scintillation indices (34) and (35) depend on the mapping function $\sec\theta_r$, which diverges as $\theta_r \to 90^\circ$.

One also notes the difference in the position of the regions of enhanced S_4 for the flat- and spherical geometry approximations at large zenith angles. For the flat-geometry approximation the maximal value of the enhancement is obtained for the dip angle $\psi = 0^\circ$. In the case of the spherical-geometry approximation the region of enhanced scintillation shifts to finite values of the dip angle. This happens because the correlation ellipsoid should be inclined to the local horizontal plane at the scattering point in order that the propagation path, horizontal for the receiver, would cross the ellipsoid along the major semi-axis. This is a purely geometric effect that is related to the finiteness of the radii of curvature of the Earth surface and of the ionospheric shell.

In Fig. 3 and in the following figures we have set the irregularity strength parameter to be the constant with the value $C_s\Delta h = 4.77 \times 10^{22}\mathrm{m}^{-p-4}$ with p being the spectral index. By doing so we neglect any effects connected with the morphology of $C_s\Delta h$. As a consequence, the calculated scintillation indices represent not the true scintillation levels but the geometric enhancement contributions to these levels. We also note that the chosen value for $C_s\Delta h$ corresponds to $C_k L = 10^{33}\mathrm{m}^{-p-4}$ of the WBMOD model, which is approximately the value observed at the magnetic equator (Rogers et al., 2014; Mohanty et al., 2018).

Figs. 4–6 show the regions of enhanced scintillation for several link configurations on the global scale. The values for the magnetic declination, δ, and dip, ψ, angles are obtained from the International Geomagnetic Reference Field (IGRF) model of the 13th generation (Alken et al., 2021). The tilt angle γ is set to zero.

For the vertical propagation path, cf. Fig. 4, both amplitude and phase scintillation indices exhibit the geometric enhancement merely at high latitudes. At the regions near both magnetic poles the anisotropic ionospheric irregularities lie within L shells and are elongated along almost vertical direction to the ground-based observer. The signal wave is thus the worst affected by scintillation while propagating along the vertical direction. The effect of the geometric enhancement in the polar regions for the near vertical links has been previously discussed by Forte and Radicella (2004).

In another extreme case when the sender-receiver link is nearly horizontal, cf. Figs. 5 and 6, the behavior of regions of enhanced scintillation depends strongly on the receiver azimuth angle. For the azimuth angle $\phi_r = 0^\circ$ this region shifts from the northern pole towards the magnetic equator, where the orientation of field-aligned irregularities is given by small values of the geomagnetic dip angle. The exact position of this enhancement belt depends on the receiver azimuth angle and on the geometric approximation that is used. For example, by comparing Figs. 5 (a) and (b) one observes that the flat-geometry approximation, case (b), yields the enhancement belt that is shifted more towards the magnetic equator in comparison to the spherical geometry approximation result, cf. plot (a). This shift of the enhancement belt for different approximation is again connected with the difference in values of the dip angle at the receiver horizon, cf. for example Fig. 3, cases II and IV.

If the receiver azimuth angle is changed to $\phi_r = 90^\circ$ the map of the geometric enhancement of scintillation exhibits a more uniform distribution of values with some reduced scintillation levels near the magnetic poles, cf. Figs. 5 (c), (d) and 6 (c), (d). This uniformity is connected with the geometry of sender-receiver links crossing the correlation ellipsoids in the directions near or along of one of the minor semi-axes. By comparing Fig. 5 (c) with Fig. 5 (d) or the corresponding plots in Fig. 6 one can note that the regions of enhancement are almost complimentary to each other if calculated using different geometrical models. This observation shows that the accounting for the finiteness of the Earth surface curvature becomes essential for very slant propagation links and the use of the flat-geometry approximation might mislead in estimation of regions of geometrically enhanced scintillation. One can also note that the flat-geometry approximation, cf. Fig. 5 (b), (d) and 6 (b), (d), yields higher values of the scintillation index for almost horizontal links in comparison to the spherical-geometry approximation, cf. Fig. 5 (a), (c) and 6 (a), (c).

We now compare the amplitude scintillation index calculated by using the proposed spherical-geometry approximation, the flat-geometry approximation of (Rino, 1979a), and the corrected flat-geometry approximation (Priyadarshi and Wernik, 2013). The latter correction is based on Eqs. (34) and (35) where the zenith angle is adjusted in order to account for the finiteness of the Earth curvature according to Eq. (C.2) of Appendix C. Fig. 7 demonstrates the comparison of these models for the case of the wing-like irregular structures. One can see that both

[4] The negligible dependence of scintillation levels on medium correlation properties along the propagation (longitudinal) direction is explained as follows. The characteristic irregularity scale-size along the propagation direction should have comparable magnitude of the propagation distance s in order to contribute to field fluctuations at the observer site. On the other hand, the scales in the transversal direction that affect the transmitted field are of smaller size, e.g. of the order $\sqrt{\lambda s}$ (Fresnel scale) to affect the field amplitude. Clearly, the realistic longitudinal correlation radii are several magnitudes smaller than s and hence the correlation properties along the direction of wave propagation have no result on scintillation levels.

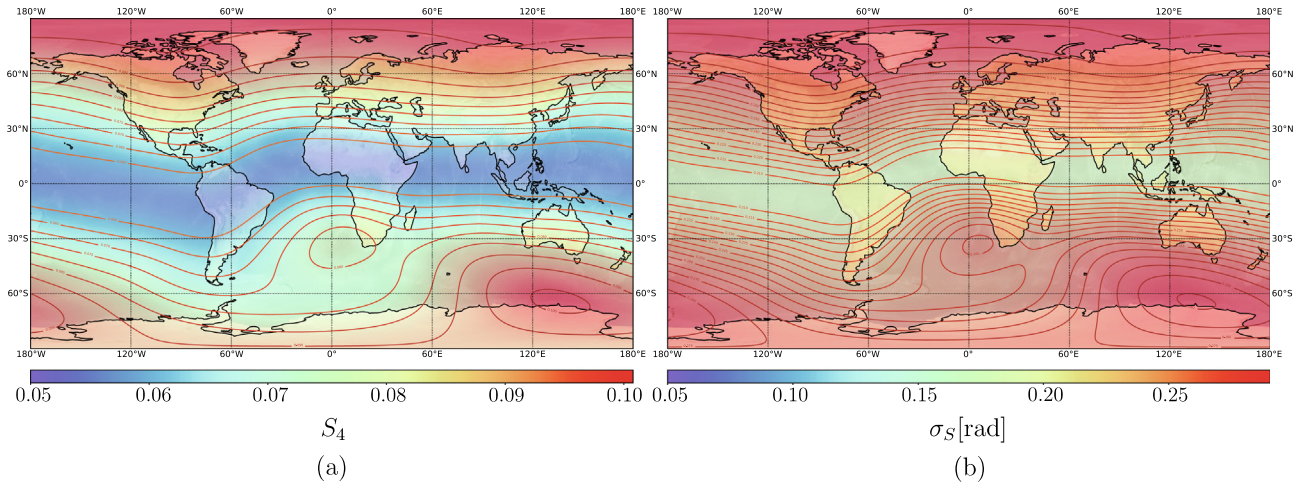

Fig. 4. Amplitude, (a), and phase, (b), scintillation indices calibrated by the condition $C_s\Delta h = \text{const}$. The indices are calculated for the zenith angle $\theta_p = \theta_r = 0$ and the azimuth angle $\phi_p = \theta_r = 0$. The height of the scattering point is taken to be equal to the ionospheric piercing point (350 km). The anisotropy parameters are set to $\alpha = 2, \beta = 1.5$.

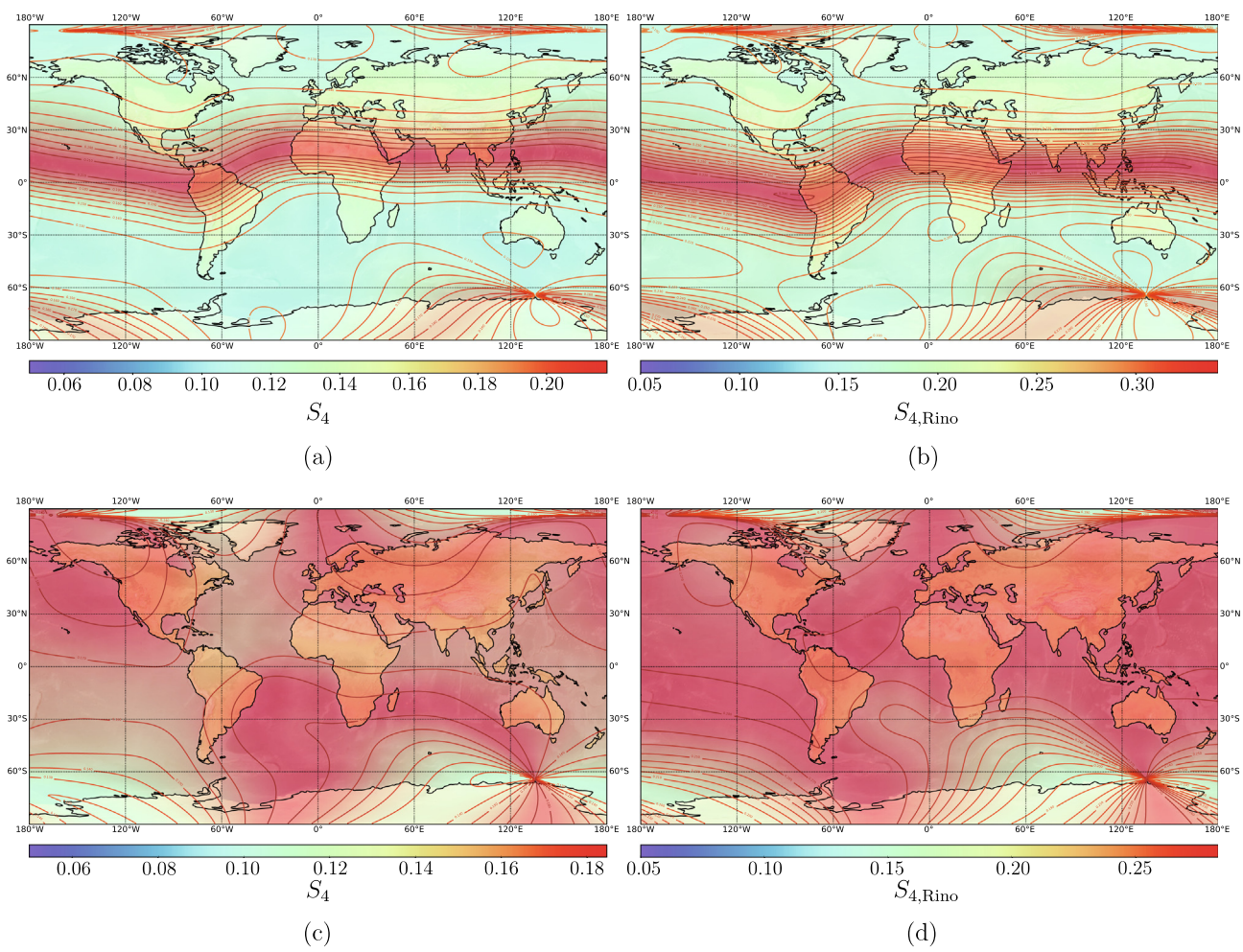

Fig. 5. Amplitude scintillation indices in the spherical-, plots (a) and (c), and in the flat-geometry approximations, plots (b) and (d). The receiver zenith angle is $\theta_r = 85^\circ$ that corresponds to the zenith angle at scattering point on plots (a) and (c) $\theta_p = 40.9^\circ$. The azimuth angles at the scattering point are: $\phi_p = 0^\circ$ for plots (a) and (b); $\phi_p = 90^\circ$ for plots (c) and (d). Other parameters are the same as for Fig. 4. Please also note the difference in ranges of values for S_4 and $S_{.4,\text{Rino}}$.

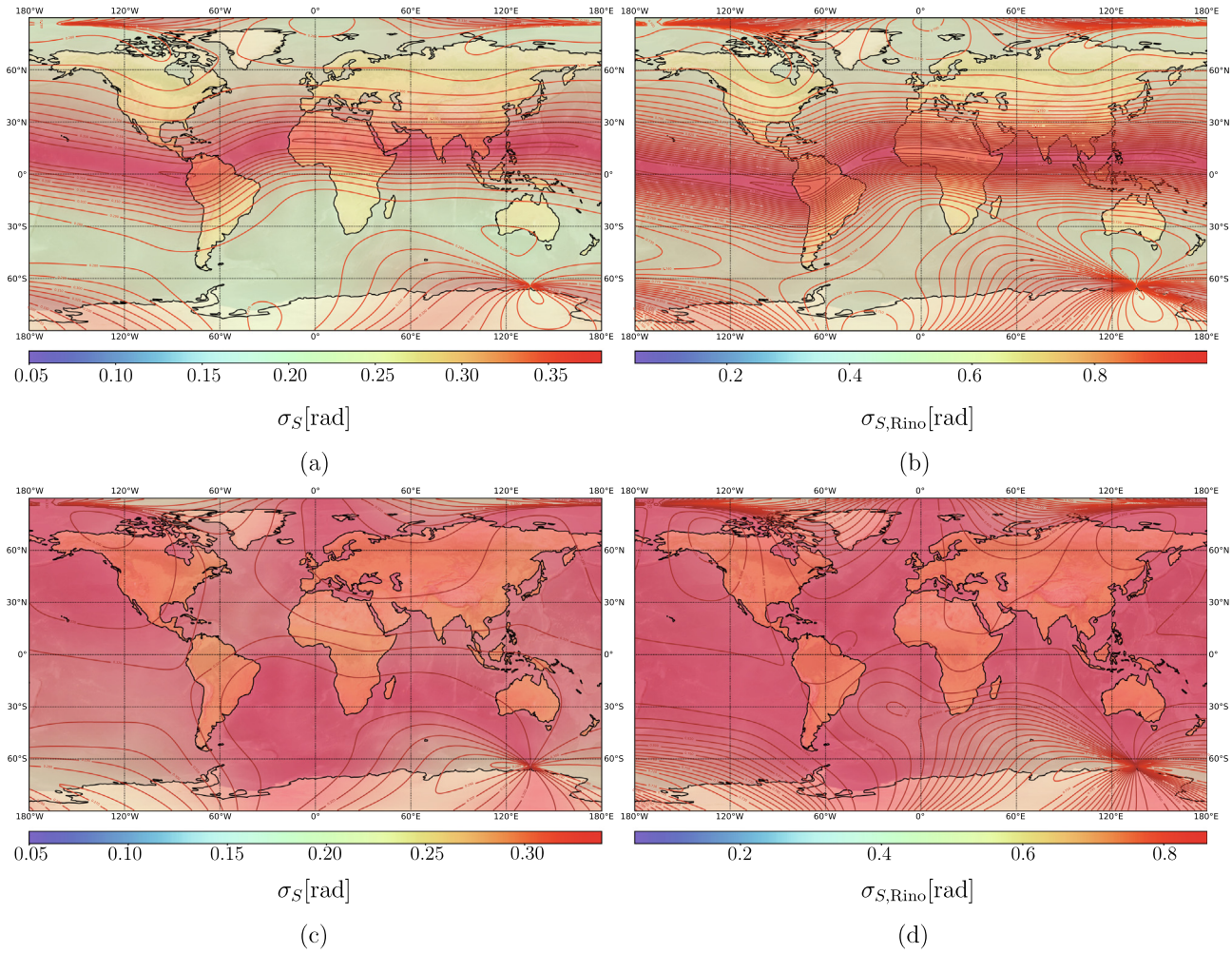

Fig. 6. Phase scintillation maps shown for the same parameters as used in Fig. 5.

flat- and spherical-geometry approximations yield comparable results for almost all values of the zenith angle. The flat-geometry approximation shows however the divergent behaviour as $\theta_r \to 90^\circ$. This is a consequence of the divergent nature of the secant as a function of the zenith angle for nearly horizontal propagation links. The corrected flat-geometry approximation according to (Priyadarshi and Wernik, 2013) does not show such a divergent character but the position of the peak of enhancement appears to be displaced in comparison to other two models. One can see that apart from the cases of nearly horizontal links all three formulations provide the comparable results.

To conclude the discussion of the geometric effect of scintillation we consider the radio communication links from a geostationary satellite over the equator broadcasting at the VHF. For this case the regions of enhanced scintillation are shown in Fig. 8. One can see two bands of geometrically enhanced amplitude scintillation situated at mid-latitudes of both Earth hemispheres. Such type of the enhancement has been discussed previously by Sinno and Minakoshi (1983), where it has been discovered that scintillation in signals from the ETS-II geostationary satellite detected in Japan are more severe than has been expected. This enhancement has been explained via the geometric effect using the theoretical formulation of (Mikkelsen et al., 1978). The calculations based on Eq. (32) reproduce the regions of enhanced scintillation in a full agreement with Sinno and Minakoshi (1983). This can be seen when comparing Fig. 8 with analogous Fig. 5 in Sinno and Minakoshi (1983). The position of the bands of enhanced scintillations at mid-latitudes is related to the link specifics between the ground receiver at these latitudes and the satellite at the geostationary orbit. While calculating the enhancement levels in Fig. 8 we assumed that each communication link with the satellite lies within the receiver meridian and the receiver position has been scanned along the longitude and latitude ranges shown in the figure. Such particular links cross the anisotropic irregularities almost along the major semi-axis at mid-latitudes, and, hence, the scintillation of the transmitted VHF signals are geometrically enhanced.

5. Conclusions

The growing range of applications that use slant and very slant signal propagation links requires the consistent

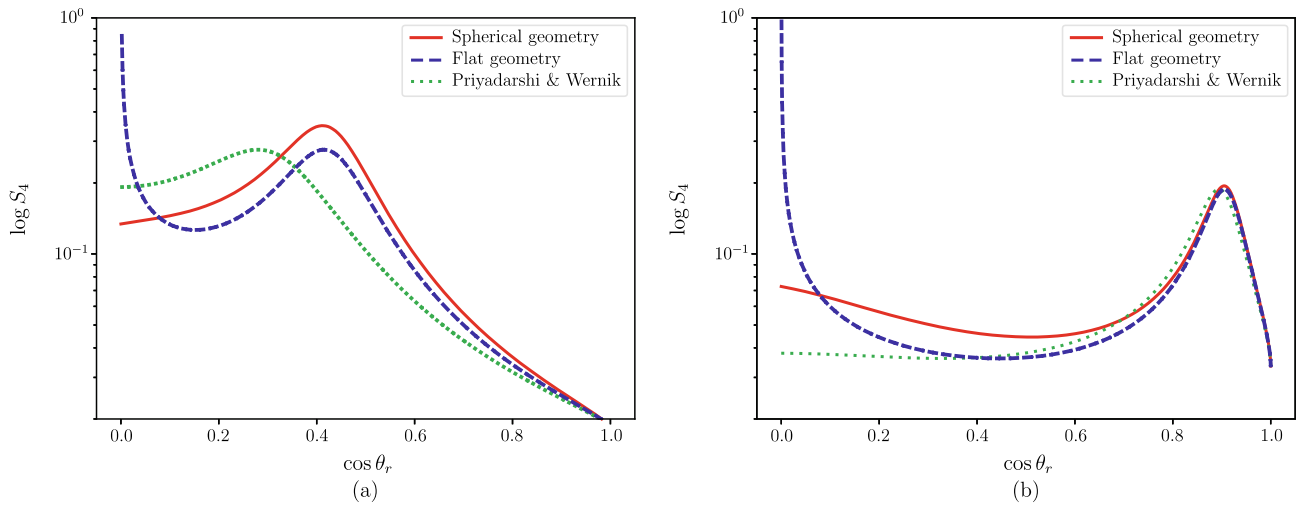

Fig. 7. Amplitude scintillation index as a function of the receiver zenith angle calculated using the spherical-geometry approximation, the flat-geometry approximation (Rino, 1979a), and the Priyadarshi and Wernik correction to the flat-geometry approximation (Priyadarshi and Wernik, 2013) for the dip angle $\psi = 25^\circ$ (a) and $\psi = 65^\circ$ (b). The parameters used in the calculation are: the spectral index $p = 1.6$, the anisotropy parameters $\alpha = 10$ and $\beta = 5$, the magnetic declination, δ, and the tilt, γ, angles are set to zero.

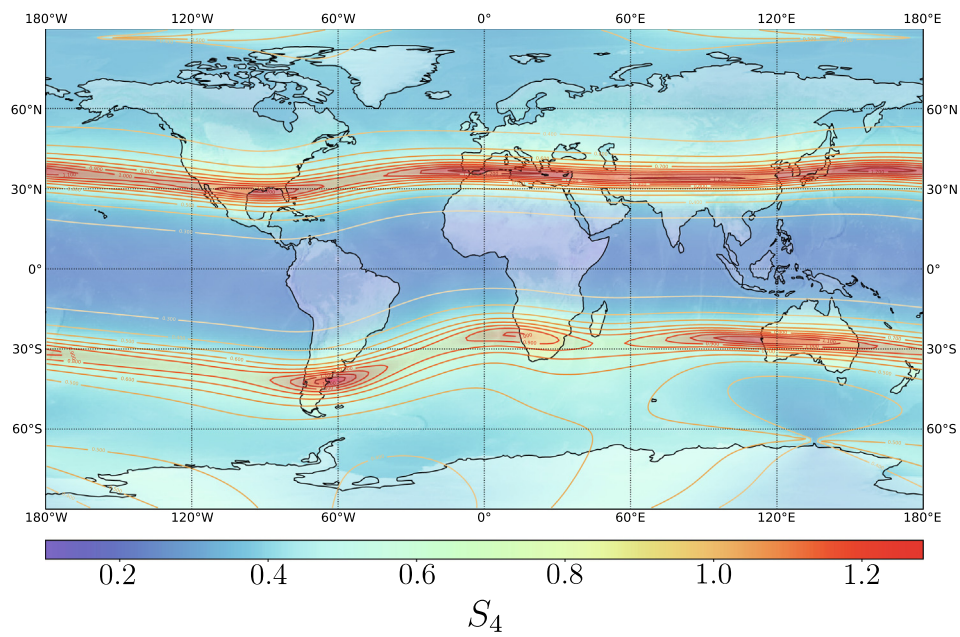

Fig. 8. Geometric enhancement of scintillation for a VHF signal from a geostationary satellite over the equator. The value of $C_s\Delta h$ is set to be constant and corresponds to the typical value at the magnetic equator. The irregularity anisotropy parameters are $\alpha = 10, \beta = 2$ and the spectral index $p = 1.6$.

accounting of the atmospheric effects for such transionospheric signal propagation geometries. In the domain of radio frequency wave propagation one of the type of signal disturbances is ionospheric scintillation, the highly variable phenomenon that depends on space weather conditions and exhibits spatial anisotropy. These features influence multiple critical services and remote sensing applications, such as the GNSS-assisted positioning and navigation (Banville and Langley, 2013; Prikryl et al., 2016; Linty et al., 2018; Yang and Morton, 2020), radio-occultation (Yakovlev et al., 1995; Anderson and Straus, 2005) and reflectometric (Semmling et al., 2014; Dielacher et al., 2022) measurements, SAR imaging and interferometry (Yakovlev et al., 1995; Anderson and Straus, 2005).

In the present article we derive the amplitude and phase scintillation indices in analytic form for the weak scattering regime taking into account the finiteness of the radius of curvature of the Earth and of the ionospheric shell. The obtained results yield the generalization of the classical Rino model of ionospheric scintillation (Rino, 1979a), which was originally formulated with the assumption that the ionospheric layer is plan-parallel and the Earth surface is flat. The presented approach differs from the Rino model in several respects.

Firstly, by accounting for spherical geometry we can also consider very slant propagation paths of transionospheric waves. In contrast to our results, the scintillation indices obtained within the flat-geometry approach exhibit the divergent behavior, the effect especially noticeable for the amplitude scintillation index S_4.

Secondly, we chose the plane of the random phase screen to be transversal to the wave propagation direction in contrast to the choice in Rino and Fremouw (1977), Rino (1979a), where the authors consider the phase screen plane to be transversal to the vertical direction of the receiver. Our choice enables one to avoid the additional projectional transformations of spatial coordinates that correct the vertical propagation case to cases with non-zero zenith angles. The absence of such transformations in our approach yields a simpler functional dependence. At the same time our formulas fully coincidence with Rino's expressions for the vertical links (zero receiver zenith angle), where both geometrical treatments should yield the same results. The particular choice of the phase screen placement yield different expressions of coefficients (B.1) and (37) due to the difference in cross-sections of phase screens with ellipsoidal surface of constant correlation for anisotropic ionospheric irregularities. This discrepancy is important to take into account that the analytic expressions of scintillation indices in both formulations look very similar.

Finally, we note, that the usage of the spherical-geometry approximation makes the proposed approach suitable for direct applications in problems involving satellite-mediated propagation links. For example, one can calculate the instantaneous position of a satellite from its Keplerian elements and using the knowledge of coordinates of the ground-based receiver to determine the coordinates of scattering point within the phase screen, for details see for Example Appendix A. This enables us to determine the model parameters such as the coefficients given by Eq. (B.1) in self consistent way. In contrast to this, the flat-geometry approximation intrinsically assumes that the local coordinates of the transmitter (satellite), receiver, and scattering point are the same. This assumption limits the integration of satellite orbiting dynamics in the flat-geometry approach.

In this study we have ignored the morphology of the irregularity strength parameter integrated over the thickness of the irregular ionosphere. Therefore we have set $C_s\Delta h = \text{const}$ in order to emphasize the purely geometric enhancement effect on scintillation levels. This morphology can be added within the WBMOD model according to Fremouw and Secan (1984); Secan et al. (1987); Secan et al. (1997) in order to obtain the global distribution of scintillation indices. One practically interesting example of geometrically enhanced scintillation is connected with the problem of the VHF signal propagation from a geostationary beacon satellite. If this satellite is located over the equator, the received signal exhibits strong scintillation at mid-latitudes, an effect reported in Sinno and Minakoshi (1983). In this region the integrated irregularity strength parameter, $C_s\Delta h$, attains almost constant and relatively low values, cf. (Rogers et al., 2014). So the characteristics that are associated with the level of disturbance of the ionospheric medium does not contribute to this scintillation enhancement effect. On the other hand, the proper accounting of the geometry of communication link and of the anisotropic field-aligned scintillation-associated irregularities explains the observed enhancement effect.

Declaration of Competing Interest

The authors declare that they have no known competing financial interests or personal relationships that could have appeared to influence the work reported in this paper.

Acknowledgments

The work was carried out within the programmatic funding of the German Aerospace Center.

Appendix A. Determination of coordinates of the scattering point

In most practical situations we know the geographic coordinates of the sender and the receiver but not those of the scattering point. Suppose we can estimate or determine the altitude of the scattering layer, h_p, i.e., by assuming that it coincides with the height of the ionospheric pierce point. With this knowledge we are able to determine the geographic or local coordinates of the scattering point with the help of the procedure outlined in this appendix.

Let the position of the scattering point be given by the vector $\mathbf{r}_p$ in some conventional terrestrial coordinate system (CTS). Similarly, let the vectors $\mathbf{r}_s$ and $\mathbf{r}_r$ denote the positions of the sender and of the receiver, respectively. Denoting the Earth radius as $R_\oplus$ we have $|\mathbf{r}_p| = R_\oplus + h_p$. Similarly we have $|\mathbf{r}_s| = R_\oplus + h_s$ and $|\mathbf{r}_r| = R_\oplus + h_r$, where h_s and h_r are the altitudes of the sender and the receiver, correspondingly[5]. The orientation of the vectors $\mathbf{r}_s, \mathbf{r}_r$ in the CTS is described by the longitudes Λ_s, Λ_r and by the corresponding latitudes Φ_s, Φ_r. The corresponding coordinates Λ_p and Φ_p of the scattering point are to be determined.

We firstly obtain the expressions for the azimuth and zenith angles. We refer to Fig. 9 for necessary geometric constructions. The angle between the vectors $\mathbf{r}_s$ and $\mathbf{r}_r$ is obtained from the cosine law for spherical triangles as

$$\cos\delta = \sin\Phi_r \sin\Phi_s + \cos\Phi_r \cos\Phi_s \cos(\Lambda_s - \Lambda_r). \tag{A.1}$$

From the triangle ORS of Fig. 9 (b) using the law of sines we derive

[5] We preserve the finite value of the receiver altitude by keeping in mind potential applications to the limb sounding links, where both the sender and the receiver are located on satellites.

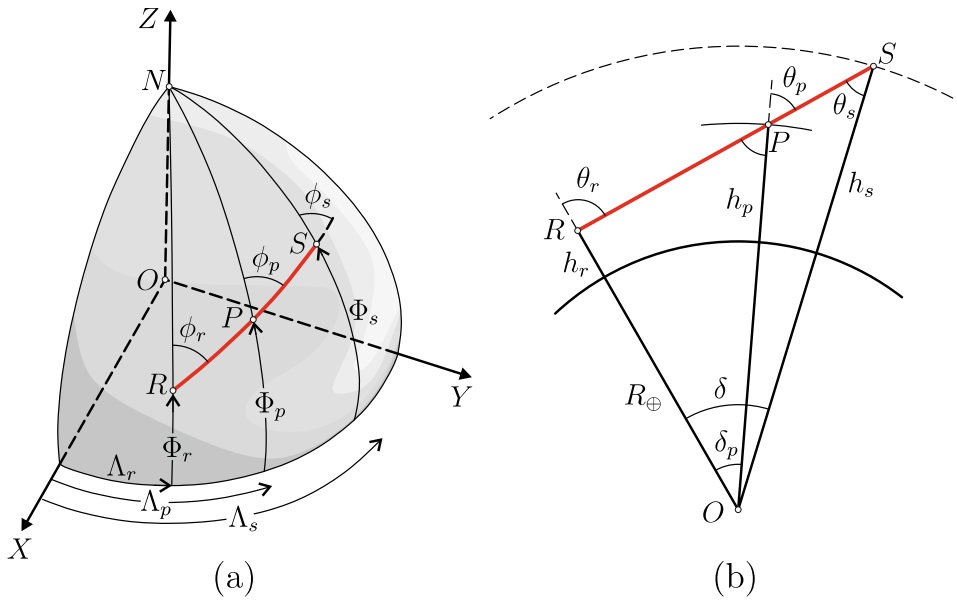

Fig. 9. Geometric constructions used for the determination of: (a) the geographic coordinates Φ_p and Λ_p as well as of the azimuth angles ϕ_r, ϕ_p, ϕ_s associated with the slant path; (b) the zenith angles θ_r, θ_p, and θ_s.

$$\frac{\sin\delta}{\ell} = \frac{\sin\theta_r}{|\mathbf{r}_s|}, \tag{A.2}$$

where

$$\ell^2 = |\mathbf{r}_s|^2 + |\mathbf{r}_r|^2 - 2|\mathbf{r}_s||\mathbf{r}_r|\cos\delta \tag{A.3}$$

is the slant range between the sender and the receiver. From the law of cosines for the triangle ORS we can also write

$$|\mathbf{r}_s|^2 = \ell^2 + |\mathbf{r}_r| + 2\ell|\mathbf{r}_r|\cos\theta_r. \tag{A.4}$$

Substituting Eqs. (A.2) and (A.3) in Eq. (A.4) one obtains for the receiver zenith angle the following expression:

$$\theta_r = \arctan\left(\frac{\sin\delta}{\cos\delta - \frac{|\mathbf{r}_r|}{|\mathbf{r}_s|}}\right) = \arctan\left(\frac{\sin\delta}{\cos\delta - \frac{R_\oplus + h_r}{R_\oplus + h_s}}\right) \tag{A.5}$$

From the spherical triangle RNS on Fig. 9 (a) we obtain by using the sine and cosine theorems:

$$\frac{\sin\phi_r}{\sin\left(\frac{\pi}{2} - \Phi_s\right)} = \frac{\sin(\Lambda_s - \Lambda_r)}{\sin\delta}, \tag{A.6}$$
$$\cos\left(\frac{\pi}{2} - \Phi_s\right) = \cos\delta\sin\Phi_r + \sin\delta\cos\Phi_r\cos\phi_r$$

from which follows the expression for the azimuth angle for the link at the receiver location:

$$\phi_r = \arctan\left(\frac{\sin(\Lambda_s - \Lambda_r)\cos\Phi_r\cos\Phi_s}{\sin\Phi_s - \sin\Phi_r\cos\delta}\right). \tag{A.7}$$

On the similar footing we obtain for the zenith angle of the link at the location of the scattering point

$$\theta_p = \arctan\left(\frac{\sin\theta_r}{\sqrt{\left(\frac{R_\oplus + h_p}{R_\oplus + h_r}\right)^2 - \sin^2\theta_r}}\right). \tag{A.8}$$

For the azimuth angle at the scattering point location we use the half-angle formula for the spherical triangle RNP that yields

$$\phi_p = \pi - 2 \times \arctan\left(\left\{\frac{\sin\left[\frac{1}{2}(\delta_p + \Phi_p - \Phi_r)\right]}{\sin\left[\frac{1}{2}(\delta_p - \Phi_p + \Phi_r)\right]}\frac{\cos\left[\frac{1}{2}(\delta_p + \Phi_p + \Phi_r)\right]}{\cos\left[\frac{1}{2}(\delta_p - \Phi_p - \Phi_r)\right]}\right\}^{\frac{1}{2}}\right), \tag{A.9}$$

where

$$\delta_p = \theta_r - \theta_p \tag{A.10}$$

is the angle between the vectors $\mathbf{r}_r$ and $\mathbf{r}_p$ and

$$\Phi_p = \frac{\pi}{2} - \arccos\left(\sin\Phi_r\cos\delta_p + \cos\Phi_r\sin\delta_p\cos\phi_r\right) \tag{A.11}$$

is the geographic latitude at the scattering point. The latter expression is obtained from the cosine law for the spherical triangle RNP. Finally, using the cosine theorem for the spherical triangle RNP we obtain the geographic longitude of the scattering point as

$$\Lambda_p = \Lambda_r + \arctan\left(\frac{\sin\phi_r\sin\delta_p\cos\Phi_r}{\cos\delta_p - \sin\Phi_p\sin\Phi_r}\right). \tag{A.12}$$

Eqs. (A.8), (A.9), (A.11), (A.12) determine the unknown geographic and local coordinates of the scattering point provided its height above the ground is known.

For the sake of completeness we also list the formulas for the zenith and azimuth angles of the link at the sender

location. On the similar footing as the expressions (A.5) and (A.7) have been derived we obtain

$$\theta_s = \arctan\left(\frac{\sin\delta}{\frac{R_\oplus+h_s}{R_\oplus+h_r} - \cos\delta}\right), \tag{A.13}$$

$$\phi_s = \arctan\left(\frac{\sin(\Lambda_s - \Lambda_r)\cos\Phi_r\cos\Phi_s}{\sin\Phi_s\cos\delta - \sin\Phi_r}\right), \tag{A.14}$$

where δ is given in Eq. (A.1).

We finally determine the distance between the scattering point and the receiver, which we denote $s = \overline{PR}$, cf. Fig. 9 (b). Using the cosine theorem for the triangle ORS we obtain

$$s = \sqrt{(R_\oplus + h_r)^2 + (R_\oplus + h_p)^2 - 2(R_\oplus + h_r)(R_\oplus + h_p)\cos\delta_p}, \tag{A.15}$$

where δ_p is given by Eq. (A.10).

Appendix B. Calculation of autocorrelation function in the local coordinates of the receiver

The autocorrelation functions for the log-amplitude and phase fluctuations, cf. Eqs. (13), (14), have been obtained as the functions of the spatial coordinates associated with the direction of radio wave propagation. In this case the z variable is counted along the direction of propagation, while the spatial variable $\mathbf{r}_\perp$ is transversal to this direction. The components of the vector $\mathbf{r}_\perp$ are defined in the xy coordinate plane, where the x-axis lies in the plane associated with the communication link, cf. Fig. 2. For the calculation of scintillation indices, the autocorrelation functions have been taken at $z = s$ and $\mathbf{r}_\perp = 0$ with s being the slant range from the scattering irregularity to the receiver station. If one is interested in the correlation analysis of the phase and log-amplitude fluctuations, the variable $\mathbf{r}_\perp$ should be kept finite. Moreover, the receiver of the signal usually performs the correlation analysis for quantities measured within the plane perpendicular to the local vertical direction. Thus, it is essential to perform transformation from variables $\mathbf{r}_\perp, z$ to the variables associated with the receiver correlation plane (Khudukon et al., 1994).

Let us consider for definiteness the correlation function for the log-amplitude fluctuations. Substituting Eq. (8) in Eq. (10) one obtains

$$\begin{aligned}\rho_\chi(\mathbf{r}_1,\mathbf{r}_2) = {} & \tfrac{k^2}{4\pi^2}\int \rho_{\delta\varphi}\left(\mathbf{r}'_{1,\perp} - \mathbf{r}'_{2,\perp}\right) \\ & \times \tfrac{1}{z_1}\cos\left(\tfrac{k}{2z_1}|\mathbf{r}_{1,\perp} - \mathbf{r}'_{1,\perp}|^2\right) \\ & \times \frac{1}{z_2}\cos\left(\frac{k}{2z_2}|\mathbf{r}_{2,\perp} - \mathbf{r}'_{2,\perp}|^2\right)\mathrm{d}^2\mathbf{r}'_{1,\perp}\mathrm{d}^2\mathbf{r}'_{2,\perp}.\end{aligned} \tag{B.1}$$

Using the spectral representation of the correlation function $\rho_{\delta\varphi}$ this integral can be reduced to the following form:

$$\begin{aligned}\rho_\chi(\mathbf{r}_\perp, z_1, z_2) = {} & \tfrac{1}{2}\int \Phi_{\delta\varphi}(\boldsymbol{\kappa}_\perp)\, e^{i\boldsymbol{\kappa}_\perp\cdot\mathbf{r}_\perp}\left[\cos\left(\tfrac{z_1-z_2}{2k}\kappa_\perp^2\right)\right. \\ & - \left.\cos\left(\tfrac{z_1+z_2}{2k}\kappa_\perp^2\right)\right]\mathrm{d}^2\boldsymbol{\kappa}_\perp,\end{aligned} \tag{B.2}$$

where $\mathbf{r}_\perp = \mathbf{r}_{1,\perp} - \mathbf{r}_{2,\perp}$. The expression (B.2) reduces to Eq. (13) by setting $z_1 = z_2 = s$.

Let us now express the autocorrelation (B.2) in terms of the spatial variables defined in the conventional receiver coordinates. Let us denote the NED coordinate system of the receiver as X, Y, Z and assume that one value of log-amplitude for correlation analysis is measured at the center of this coordinate system. This value is correlated then with the log-amplitude value measured in XY plane at the point which position is determined by the vector $\mathbf{R}_\perp$. Clearly, the vector $\mathbf{R}_\perp$ is the vector $\mathbf{r}_\perp$ projected on the plane XY. The components r_x, r_y of the vector $\mathbf{r}_\perp$ can be expressed in terms of the components of the vector $\mathbf{R}_\perp$ as

$$r_x = \cos\theta_r(R_X\cos\phi_r - R_Y\sin\phi_r), \qquad r_y = R_X\sin\phi_r + R_Y\cos\phi_r,$$

where θ_r and ϕ_r are the zenith and azimuth angles of the receiver respectively. If one performs the correlation analysis within the receiver correlation plane, one needs to account now that $z_1 \neq z_2$. If z_1 is chosen to be equal to the slant range, i.e.,

$$z_1 = s, \tag{B.4}$$

then the value of z_2 is determined as

$$z_2 = s + \sqrt{R_x^2 + R_y^2}\tan\omega, \tag{B.5}$$

where

$$\omega = \arccos\left(\frac{\tau}{\sqrt{R_x^2 + R_y^2}}\right), \tag{B.6}$$

$$\begin{aligned}\tau = {} & (R_x^2(\cos^2\theta_r\cos^2\phi_r + \sin^2\phi_r) \\ + {} & R_y^2(\cos^2\theta_r\sin^2\phi_r + \cos^2\phi_r) \\ + {} & R_xR_y\sin^2\theta_r\sin 2\phi_r)^{\frac{1}{2}}\end{aligned}$$

is the angle between the vectors $\mathbf{R}$ and $\mathbf{r}_\perp$. Substitution of Eqs. (B.3)–(B.5) in Eq. (B.2) yields the expression of the log-amplitude correlation as the function of the distance vector $\mathbf{R}$ defined in the receiver plane.

Appendix C. Mapping function from vertical to slant propagation path lengths

In this appendix we derive the expression for the mapping function M that enables one to express the slant lengths in terms of the corresponding lengths defined along some vertical direction. Firstly, we derive the mapping function when the vertical direction is taken to coincide with the vertical at the receiver location. In this case M is the function of the receiver zenith angle θ_r, that is the measure of how the slant path is inclined relative to the vertical, cf. Fig. 9 (b). Using simple geometric considerations, the length element along the slant direction, ds, can be expressed in terms of the length element along the receiver vertical, dh, as

$$\mathrm{d}s = \frac{\mathrm{d}h}{\sqrt{1-\left(\frac{R_\oplus+h_r}{R_\oplus+h}\right)^2 \sin^2\theta_r}}, \tag{C.1}$$

where for explanation of the notations we refer to Appendix A and Fig. 9 (b). Comparing Eq. (C.1) with the analogous expression written in terms of the local zenith angle θ, i.e., $\mathrm{d}s = \sec\theta \mathrm{d}h$, one obtains another useful formula

$$\theta = \arccos\left(\sqrt{1-\left(\frac{R_\oplus+h_r}{R_\oplus+h}\right)^2 \sin^2\theta_r}\right). \tag{C.2}$$

This angle is defined at the height h above the ground level for a point on the slant path inclined on angle θ_r to the receiver vertical direction.

We consider now the spherical shell of the thickness Δh with center at the center of the Earth. The outer radius of the shell is $R_\oplus + h_p$ and the inner radius is correspondingly $R_\oplus + h_p - \Delta h$. The slant thickness of the shell along the path that connects the scattering point P and the receiver R follows from (C.1) as

$$\Delta s = \int_0^{\Delta s} \mathrm{d}s = \int_{h_p-\Delta h}^{h_p} \frac{\mathrm{d}h}{\sqrt{1-\left(\frac{R_\oplus+h_r}{R_\oplus+h}\right)^2 \sin^2\theta_r}}. \tag{C.3}$$

Performing the integration in the right side of the equation, one obtains

$$\begin{aligned} \Delta s &= \Delta h \cdot M(\theta_r), \\ M(\theta_r) &= \sqrt{\xi^2\cos^2\theta_r + 2\xi\zeta + \zeta^2} \\ &- \sqrt{\xi^2\cos^2\theta_r + 2\xi(\zeta-1) + (\zeta-1)^2}, \end{aligned} \tag{C.4}$$

where $\xi = (R_\oplus + h_r)/\Delta h$ and $\zeta = (h_p - h_r)/\Delta h$.

Here we also derive the expression for M as the function of the zenith angle of the scattering point θ_p. Applying the sine theorem to the triangle ORP on Fig. 9 (b), one obtains

$$\cos\theta_r^2 = 1 - \left(\frac{R_\oplus+h_p}{R_\oplus+h_r}\right)^2 \sin^2\theta_p. \tag{C.5}$$

Inserting this equation in Eq. (C.4) one derives

$$\begin{aligned} \Delta s &= \Delta h \cdot M(\theta_p), \\ M(\theta_p) &= \tilde{\xi}\cos\theta_p - \sqrt{\tilde{\xi}^2\cos^2\theta_p - 2\tilde{\xi} + 1}, \end{aligned} \tag{C.6}$$

where $\tilde{\xi} = (R_\oplus + h_p)/\Delta h$. Here we note that while the zenith angle of the receiver is defined in the range $[0, \pi/2]$, the zenith angle at the scattering point at the same time varies in the range $\left[0, \theta_p^{\max}\right]$, where

$$\theta_p^{\max} = \arccos\left(\tilde{\xi}^{-1}\sqrt{2\tilde{\xi}-1}\right). \tag{C.7}$$

The maximal slant thickness of the spherical shell at this angle is

$$\Delta s^{\max} = \sqrt{\Delta h^2 + 2\Delta h\left(R_\oplus + h_p - \Delta h\right)}.$$

In order to complete the discussion of the mapping functions, we express the slant range s in terms of the receiver zenith angle and in terms of the vertical height from the receiver to the scattering point, i.e., in terms of $h_p - h_r$. This dependence can be again represented in terms of the mapping function $\overline{M}$, where

$$\begin{aligned} s &= \left(h_p - h_r\right) \cdot \overline{M}(\theta_r), \\ \overline{M}(\theta_r) &= \sqrt{\overline{\xi}^2\cos^2\theta_r + 2\overline{\xi} + 1} - \overline{\xi}\cos\theta_r, \\ \overline{\xi} &= (R_\oplus + h_r)/\left(h_p - h_r\right). \end{aligned} \tag{C.8}$$

These expressions one obtains directly from Eq. (C.6) via the replacement $\Delta h \to h_p - h_r$. Similarly, Eq. (C.6) can be used to express the slant range in terms of the zenith angle of the scattering point. The slant range representation (C.8) is an alternative to the formula (A.15).

Appendix D. On the relationship between power spectral densities.

In this appendix we derive Eq. (15) and comment on the analogous relationship for the case of the plan-parallel ionosphere. Consider the correlation function of phase fluctuations of the phase screen determined at two spatial points. The positions of the points are given by the vectors $\mathbf{r}_{1,\perp}$ and $\mathbf{r}_{2,\perp}$. These vectors lie in the plane of the phase screen and with the origins at the cross-section point of the signal ray and the phase screen. In the following we assume that the medium is spatially homogeneous. Substituting Eq. (6) in Eq. (10) and denoting $\mathbf{r}_\perp = \mathbf{r}_{1,\perp} - \mathbf{r}_{2,\perp}$ we obtain

$$\rho_{\delta\varphi}(\mathbf{r}_\perp) = \lambda^2 r_e^2 \int_0^{\Delta s}\int_0^{\Delta s} \rho_{\delta N_e}(\mathbf{r}_\perp, z_1 - z_2)\mathrm{d}z_1\mathrm{d}z_2, \tag{D.1}$$

where Δs is the slant thickness of the ionospheric layer. Transforming the integration variables according to $z = z_1 - z_2, Z = (z_1 + z_2)/2$ one can perform the integration over Z variable explicitly. Using the spectral representation of the correlation functions in Eq. (D.1) one derives

$$\int_{\mathbb{R}^2} \Phi_{\delta\varphi}(\boldsymbol{\kappa}_\perp) e^{i\boldsymbol{\kappa}_\perp\cdot\mathbf{r}_\perp} \mathrm{d}^2\boldsymbol{\kappa}_\perp \tag{D.2}$$

$$\lambda^2 r_e^2 \Delta s \int_{-\Delta s}^{\Delta s}\int_{\mathbb{R}^3} \Phi_{\delta N_e}(\boldsymbol{\kappa}_\perp, \kappa_z) e^{i\boldsymbol{\kappa}_\perp\cdot\mathbf{r}_\perp + i\kappa_z z} \mathrm{d}z\,\mathrm{d}^2\boldsymbol{\kappa}_\perp\,\mathrm{d}\kappa_z,$$

where the slant thickness of the spherical shell Δs is related to the shell thickness with the help of the mapping function as given in Eqs. (C.4) and (C.6). Integration of Eq. (D.2) with respect to κ_z yields then the required formula (15).

For the plan-parallel model of the ionospheric layer considered in (Rino and Fremouw, 1977; Rino, 1979a) the Eq. (D.2) can be written as

$$\int_2 \Phi_{\delta\varphi}(\boldsymbol{K}_\perp) e^{i\boldsymbol{K}_\perp\cdot\mathbf{R}_\perp} \mathrm{d}^2\boldsymbol{K}_\perp \tag{D.3}$$

$$= \lambda^2 r_e^2 \Delta s \int_{-\Delta s}^{\Delta s} \int_3 \Phi_{\delta N_e}(\boldsymbol{K}_\perp, K_h) e^{i\boldsymbol{K}_\perp \cdot (\mathbf{R}_\perp + \tan\theta \boldsymbol{a}_{k,\perp} h)} \times e^{iK_h h} \mathrm{d}(h \sec\theta)\, \mathrm{d}^2\boldsymbol{K}_\perp \mathrm{d}K_h,$$

where $\mathbf{R}_\perp$ is the spatial vector lying in the plane of the ground observer, cf. Appendix B, h is the spatial variable counted along the receiver vertical starting from the position of the scattering point, and $\boldsymbol{a}_{k,\perp} = \sin\theta(\cos\phi \quad \sin\phi)^T$ is the transversal component of the unit vector $\boldsymbol{a} = \boldsymbol{k}/k$ with $\boldsymbol{k}$ being the wave vector of the signal wave. It is worth mentioning that due to the flat geometry, the zenith, θ, and azimuth, ϕ, angles for the sender, the scattering point, and the receiver attain the same values in contrast to the case of the spherical geometry. The slant thickness of the plan-parallel ionospheric slab is $\Delta s = \Delta h \sec\theta$ with Δh being the slab thickness. The shift of the spatial vector $\mathbf{R}_\perp$ to $\mathbf{R}_\perp + \tan\theta \boldsymbol{a}_{k,\perp} h$ accounts the displacement of the center of the receiver coordinate system relative to the projection of the scattering point on the flat-Earth surface.

Integration of Eq. (D.3) with respect to h and K_h yields

$$\Phi_{\delta\varphi}(\boldsymbol{K}_\perp) = 2\pi\lambda^2 r_e^2 \Delta h (\sec\theta)^2 \Phi_{\delta N_e}(\boldsymbol{K}_\perp, -\tan\theta \boldsymbol{K}_\perp \cdot \boldsymbol{a}_{k,\perp}). \tag{D.4}$$

If we compare Eq. (D.4) with Eq. (15), we observe that the constant factors on the right hand sides of these equations have different dependencies on the horizontal-to-slant mapping functions. In the case of the spherical geometry this factor is proportional to the mapping function (C.4) [alternatively given by Eq. (C.6)], while for the flat geometry this factor is proportional to the second power of the corresponding mapping function, i.e., to $(\sec\theta)^2$.

Appendix E. Calculation of integrals in Eqs. (29) and (30)

The integrals appearing in Eqs. (29), (30) have been calculated in Rino (1979a). In the sake of completeness we outline the integration procedure in this appendix.

Consider firstly the integral

$$\mathscr{I}_1 = \int_{\mathbb{R}^2} \frac{\mathrm{d}\kappa_x \mathrm{d}\kappa_y}{\left(\mathscr{A}\kappa_x^2 + 2\mathscr{B}\kappa_x\kappa_y + \mathscr{C}\kappa_y^2 + r_0^2\kappa_0^2\right)^{\frac{p+2}{2}}}. \tag{E.1}$$

We now perform the coordinate transformation in Eq. (E.1) that brings the quadratic form (25) to the diagonal representation according to:

$$\begin{aligned} \kappa_x &= \tfrac{\mathscr{A}-\mathscr{C}+\mathscr{D}}{2\sqrt{\mathscr{B}\mathscr{D}}} q_x + \tfrac{\mathscr{A}-\mathscr{C}-\mathscr{D}}{2\sqrt{\mathscr{B}\mathscr{D}}} q_y, \\ \kappa_y &= \sqrt{\tfrac{\mathscr{B}}{\mathscr{D}}}(q_x + q_y), \end{aligned} \tag{E.2}$$

where $\mathscr{D} = \sqrt{(\mathscr{A}-\mathscr{C})^2 + 4\mathscr{B}^2}$. The Jacobian of this transformation is equal to one. The integral (E.1) can be written in terms of the new variables as

$$\mathscr{I}_1 = \int_{\mathbb{R}^2} \frac{\mathrm{d}q_x \mathrm{d}q_y}{\left(aq_x^2 + bq_y^2 + r_0^2\kappa_0^2\right)^{\frac{p+2}{2}}}, \tag{E.3}$$

where

$$\begin{aligned} a &= \frac{1}{2\mathscr{B}}\left[2\mathscr{B}^2 + \mathscr{A}(\mathscr{A}-\mathscr{C}+\mathscr{D})\right], \\ b &= -\frac{1}{2\mathscr{B}}\left[2\mathscr{B}^2 + \mathscr{A}(\mathscr{A}-\mathscr{C}-\mathscr{D})\right]. \end{aligned} \tag{E.4}$$

By rescaling the integration variables and switching to the polar coordinates this integral reduces to

$$\begin{aligned} \mathscr{I}_1 &= \tfrac{\pi}{\sqrt{\mathscr{A}\mathscr{C}-\mathscr{B}^2}} \int_0^\infty \left(x + r_0^2\kappa_0^2\right)^{-\frac{p+2}{2}} \mathrm{d}x \\ &= \tfrac{2\pi}{\sqrt{\mathscr{A}\mathscr{C}-\mathscr{B}^2}} \tfrac{1}{p} (r_0\kappa_0)^{-p}. \end{aligned} \tag{E.5}$$

Inserting Eq. (E.5) in (29) yields the phase scintillation index (31).

We now switch to the calculation of the integral

$$\mathscr{I}_2 = \int_{\mathbb{R}^2} \frac{\sin^2\left[s\left(\kappa_x^2 + \kappa_y^2\right)/2k\right]}{\left(\mathscr{A}\kappa_x^2 + 2\mathscr{B}\kappa_x\kappa_y + \mathscr{C}\kappa_y^2\right)^{\frac{p+2}{2}}} \mathrm{d}\kappa_x \mathrm{d}\kappa_y \tag{E.6}$$

which is used for calculation of the amplitude scintillation index (32). Performing the variable transformation (Appendix E) this integral is modified to

$$\mathscr{I}_2 = \int_{\mathbb{R}^2} \frac{\sin^2\left[s\left(\underline{a}q_x^2 + \underline{b}q_y^2\right)/2k\right] \mathrm{d}q_x \mathrm{d}q_y}{\left(aq_x^2 + bq_y^2\right)^{\frac{p+2}{2}}}, \tag{E.7}$$

where

$$\begin{aligned} \underline{a} &= \frac{1}{2\mathscr{B}}(\mathscr{D} + \mathscr{A} - \mathscr{C}), \\ \underline{b} &= \frac{1}{2\mathscr{B}}(\mathscr{D} - \mathscr{A} + \mathscr{C}). \end{aligned} \tag{E.8}$$

Performing the rescaling of the variables $q_x' = \underline{a}q_x, q_y' = \underline{b}q_y$ and using the polar coordinates the integral can be written as

$$\begin{aligned} \mathscr{I}_2 = \frac{1}{2}\int_0^\infty t^{-\frac{p}{2}-1} \sin^2\left(\frac{st}{2k}\right) \mathrm{d}t \int_0^{2\pi} \\ \times \frac{\mathrm{d}\phi}{\left(\frac{\underline{a}}{\underline{a}} - \left(\frac{\underline{a}}{\underline{a}} - \frac{\underline{b}}{\underline{b}}\right)\sin^2\phi\right)^{\frac{p+2}{2}}}. \end{aligned} \tag{E.9}$$

Integrating over t one obtains after some simplifications (Prudnikov et al., 1992):

$$\begin{aligned} \mathscr{I}_2 &= \tfrac{\sqrt{\pi}}{2}\left(\tfrac{s}{2k}\right)^{\frac{p}{2}} \tfrac{1}{p} \tfrac{\Gamma\left(1-\frac{p}{4}\right)}{\Gamma\left(\frac{1}{2}+\frac{p}{4}\right)} \\ &\int_0^{2\pi} \tfrac{\mathrm{d}\phi}{\left(\frac{1}{2}(\mathscr{A}+\mathscr{C}+\mathscr{D}) - \mathscr{D}\sin^2\phi\right)^{\frac{p+2}{2}}}. \end{aligned} \tag{E.10}$$

Changing the integration variable as $x = \sin^2\phi$ one can see that the integral attains the form of the Euler integral representation of the hypergeometric function ${}_2F_1(a,b;c;z)$

$$\begin{aligned}\mathscr{I}_2 = \quad & \pi^{\frac{3}{2}}\left(\frac{s}{2k}\right)^{\frac{p}{2}}\frac{1}{p}\frac{\Gamma\left(1-\frac{p}{4}\right)}{\Gamma\left(\frac{1}{2}+\frac{p}{4}\right)}\left[\frac{1}{2}\left(\mathscr{A}+\mathscr{B}+\mathscr{C}\right)\right]^{-\frac{p+2}{2}} \\ \times \quad & {}_2F_1\left(\frac{p+2}{2},\frac{1}{2};1;\frac{2\mathscr{D}}{\mathscr{A}+\mathscr{C}+\mathscr{D}}\right).\end{aligned} \tag{E.11}$$

Using the Euler transformation ${}_2F_1(a,b;c;z) = (1-z)^{c-a-b}{}_2F_1(c-a,c-b;c;z)$ and the formula

$$\begin{aligned}{}_2F_1(a,b;c;z) = \quad & 2^{2b-1}\Gamma(b+1/2)z^{\frac{1}{2}-b}(1-z)^{(2b-2a-1)/4} \\ \times \quad & P^{1/2-b}_{a-b-1/2}\left(\frac{2-z}{2\sqrt{1-z}}\right),\end{aligned}$$

where $P^{\beta}_{\alpha}(z)$ is the Legendre function, Eq. (E.11) can be written in the form

$$\begin{aligned}\mathscr{I}_2 = \pi^{\frac{3}{2}}\left(\frac{s}{2k}\right)^{\frac{p}{2}}\frac{1}{p} \\ \times \frac{\Gamma\left(1-\frac{p}{4}\right)}{\Gamma\left(\frac{1}{2}+\frac{p}{4}\right)}\left(\frac{1}{\sqrt{\mathscr{A}\mathscr{C}-\mathscr{B}^2}}\right)^{\frac{p+2}{2}}P_{\frac{p}{2}}\left(\frac{\mathscr{A}+\mathscr{C}}{2\sqrt{\mathscr{A}\mathscr{C}-\mathscr{B}^2}}\right).\end{aligned} \tag{E.12}$$

This result is used for calculation of the scintillation index given by Eq. (32).

References

Afraimovich, E.L., Ishin, A.B., Tinin, M.V., et al., 2011. First evidence of anisotropy of GPS phase slips caused by the mid-latitude field-aligned ionospheric irregularities. Adv. Space. Res. 47, 1674–1680. https://doi.org/10.1016/j.asr.2011.01.015.

Alken, P., Thébault, E., Beggan, C.D., et al., 2021. International geomagnetic reference field: the thirteenth generation. Earth, Planets Space 73 (49), 1–25. https://doi.org/10.1186/s40623-020-01288-x.

Anderson, P.C., Straus, P.R., 2005. Magnetic field orientation control of GPS occultation observations of equatorial scintillation. Geophys. Res. Lett. 32, L21107. https://doi.org/10.1029/2005GL023781.

Banville, S., Langley, R.B., 2013. Mitigating the impact of ionospheric cycle slips in GNSS observations. J. Geodet. 87, 179–193. https://doi.org/10.1007/s00190-012-0604-1.

Belcher, D., Mannix, C.R., Cannon, P.S., 2017. Measurement of the ionospheric scintillation parameter C_kL from SAR images of clutter. IEEE Trans. Geosci. Remote Sens. 55, 5937–5943. https://doi.org/10.1109/TGRS.2017.2717081.

Bezler, I., Ishin, A.B., Konetskaya, E.V., et al., 2019. Effect of anisotropy of ionospheric inhomogeneities in the detection of faults in phase GNSS measurements. Geomag. Aeron. 59, 342–350. https://doi.org/10.1134/S0016793219030046.

Bhattacharyya, A., Yeh, K.C., Franke, S.J., 1992. Deducing turbulence parameters from transionospheric scintillation measurements. Space Sci. Rev. 61, 335–386. https://doi.org/10.1007/BF00222311.

Booker, H.G., Ratcliffe, J.A., Shinn, D.H., 1950. Diffraction from an irregular screen with applications to ionospheric problems. Phil. Trans. Roy. Soc., A 242, 579–607. https://doi.org/10.1098/rsta.1950.0011.

Briggs, B.H., Parkin, I.A., 1963. On the variation of radio star and satellite scintillations with zenith angle. J. Atm. Terr. Phys. 25, 339–366. https://doi.org/10.1016/0021-9169(63)90150-8.

Briggs, B.H., Phillips, G.J., Shinn, D.H., 1950. The analysis of observations on spaced receivers of the fading of radio signals. Proc. Phys. Soc. B 63, 106–121. https://doi.org/10.1088/0370-1301/63/2/305.

Carrano, C., Groves, K.M., Rino, C.L., 2019. On the relationship between the rate of change of total electron content index (ROTI), irregularity s trength (C_kL), and the scintillation index (S_4). J. Geophys. Res. 124, 2099–2112. https://doi.org/10.1029/2018JA026353.

Carrano, C.S., Groves, K.M., Caton, R.G., 2012a. Simulating the impacts of ionospheric scintillation on L band SAR image formation. Radio Sci. 47, RS0L20. https://doi.org/10.1029/2011RS004956.

Carrano, C.S., Groves, K.M., Caton, R.G., 2012b. The effect of phase scintillations on the accuracy of phase screensimulation using deterministic screens derived from GPSand ALTAIR measurements. Radio Sci. 47, RS0L25. https://doi.org/10.1029/2011RS004958.

Carter, B.A., Retterer, J.M., Yizengaw, E., et al., 2014. Using solar wind data to predict daily GPS scintillation occurrence in the African and Asian low-latitude regions. Geophys. Res. Lett. 41, 8176–8184. https://doi.org/10.1002/2014GL062203.

Cervera, M.A., Thomas, R.M., Groves, K.M., et al., 2001. Validation of WBMOD in the Southeast Asian region. Radio Sci. 36, 1559–1572. https://doi.org/10.1029/2000RS002520.

Clifford, S.F., Yura, H.T., 1974. Equivalence of two theories of strong optical scintillation. J. Opt. Soc. Am. 64, 1641–1644. https://doi.org/10.1364/JOSA.64.001641.

Conroy, J., Deshpande, K., Kunduri, B., et al., 2021. Ionospheric scintillation data inversion to characterize the structures associated with a series of polar cap patches. Radio Sci. 56. https://doi.org/10.1029/2020RS007235, e2020RS007235.

Conroy, J., Deshpande, K., Scales, W., et al., 2022. Statistical analysis of refractive and diffractive scintillation at high latitudes. Radio Sci. 57. https://doi.org/10.1029/2021RS007259, e2021RS007259.

Costa, E., Fougere, P.F., Basu, S., 1988. Cross-correlation analysis and interpretation of spaced-receiver measurements. Radio Sci. 23, 141–162. https://doi.org/10.1029/RS023i002p00141.

De Michelis, P., Consolini, G., Pignalberi, A., et al., 2021. Looking for a proxy of the ionospheric turbulence with Swarm data. Sci. Rep. 11, 6183. https://doi.org/10.1038/s41598-021-84985-1.

Deshpande, K.B., Bust, G.S., Clauer, C.R., et al., 2014. Satellite-beacon ionospheric-scintillation global model of the upper atmosphere (SIGMA) i: High-latitude sensitivity study of the model parameters. J. Geophys. Res.: Space Phys. 119, 4026–4043. https://doi.org/10.1002/2013JA019699.

Dielacher, A., Fragner, H., Koudelka, O., 2022. PRETTY – passive GNSS-Reflectometry for CubeSats. Elektrotech. Inftech. 139, 25–32. https://doi.org/10.1007/s00502-022-00993-7.

Dyson, P.L., McClure, J.P., Hanson, W.B., 1974. In situ measurements of the spectral characteristics of F region ionospheric irregularities. J. Geophys. Res. 79, 1497–1502. https://doi.org/10.1029/JA079i010p01497.

El-Arini, M.B., Conker, R.S., Albertson, T.W., et al., 1994. Comparison of real-time ionospheric algorithms for a GPS Wide-Area Augmentation System (WAAS). Navigation 41, 393–414. https://doi.org/10.1002/j.2161-4296.1994.tb01887.x.

Fante, R.L., 1975a. Electromagnetic beam propagation in turbulent medium. Proc. IEEE 63, 1669–1692. https://doi.org/10.1109/PROC.1975.10035.

Forte, B., Radicella, S.M., 2004. Geometrical control of scintillation indices: What happens for GPS satellitess. Radio Sci. 39, RS5014. https://doi.org/10.1029/2002RS002852.

Forte, B., Radicella, S.M., 2005. Comparison of ionospheric scintillation models with experimental data for satellite navigation applications. Ann. Geophys. 48, 505–514. https://doi.org/10.4401/ag-3215.

Fremouw, E.J., Larsinger, J.M., 1981. Recent high-latitude improvements in a computer-based scintillation model. In: Goodman, J.M., Clarke, F.D., Aarons, J. (Eds.), Effect of the ionosphere on radiowave systems. Naval Research Lab, Washington DC, pp. 141–154.

Fremouw, E.J., Livingston, R.C., Miller, D.A., 1980. On the statistics of scintillating signals. J. Atm. Terr. Phys. 42, 717–731. https://doi.org/10.1016/0021-9169(80)90055-0.

Fremouw, E.J., Secan, J.A., 1984. Modeling and scientific application of scintillation results. Radio Sci. 19, 687–694. https://doi.org/10.1029/RS019i003p00687.

Gola, M., Wernik, A.W., Franke, S.J., et al., 1992. Behaviour of HILAT scintillation over Spitsbergen. J. Atm. Terr. Phys. 54, 1207–1213. https://doi.org/10.1016/0021-9169(92)90146-C.

Helmboldt, J.F., Zabotin, N., 2022. An observed trend between mid-latitudes km-scale irregularities and medium-scale traveling ionospheric disturbances. Radio Sci. 57. https://doi.org/10.1029/2021RS007396, e2021RS007396.

Hewish, A., 1951. The diffraction of radio waves in passing through a phase-changing ionosphere. Proc. Roy. Soc., A 209, 81–96. https://doi.org/10.1098/rspa.1951.0189.

Hong, J., Chung, J.-K., Kim, Y.H., et al., 2020. Characteristics of ionospheric irregularities using GNSS scintillation indices measured at Jang Bogo Station, Antarctica (74.62°S, 4164.22°E). Space Weather 18. https://doi.org/10.1029/2020SW002536, e2020SW002536.

Jandieri, G., Ishimaru, A., Rawat, B., et al., 2017. Power spectra of ionospheric scintillations. Adv. Electromagn. 6, 42–51. https://doi.org/10.7716/aem.v6i4.652.

Ji, Y., Dong, Z., Zhang, Y., et al., 2022. Measuring ionospheric scintillation parameters from SAR images using phase gradient autofocus: A case study. IEEE Trans. Geosci. Remote Sens. 60, 5200212. https://doi.org/10.1109/TGRS.2020.3044657.

Kelley, M.C., Pfaff, R., Baker, K.D., et al., 1982. Simultaneous rocket probe and radar measurements of equatorial spread F—Transitional and short wavelength results. J. Geophys. Res. 87, 1575–1588. https://doi.org/10.1029/JA087iA03p01575.

Kersley, L., Pryse, S.E., Wheadon, N.S., 1988. Amplitude and phase scintillation at high latitudes over northern Europe. Radio Sci. 23, 320–330. https://doi.org/10.1029/RS023i003p00320.

Khudukon, B.Z., Tereshchenko, E.D., Galinov, A.V., et al., 1994. Determination of drift velocity and anisotropy of irregularities in the auroral ionosphere using radio source scintillation. J. Atm. Terr. Phys. 56, 93–102. https://doi.org/10.1016/0021-9169(94)90179-1.

Knight, M., Cervera, M., Finn, A., 1999. A comparison of predicted and measured GPS performance in an ionospheric scintillation environment. In: Proceedings of the 12th International Technical Meeting of the Satellite Division of The Institute of Navigation (ION GPS 1999), pp. 1437–1450.

Koster, J.R., 1963. Some measurements of the irregularities giving rise to radio-star scintillations at the equator. J. Geophys. Res. 68, 2579–2590. https://doi.org/10.1029/JZ068i009p02579.

Koster, J.R., 1972. Equatorial scintillation. Planet. Space Sci. 20, 1999–2014. https://doi.org/10.1016/0032-0633(72)90056-6.

Kumagai, H., Ogawa, T., 1986. Behavior of mid-latitude F-region irregularities deduced from spaced-receiver VHF scintillation measurements. Radio Sci. 48, 221–230. https://doi.org/10.1016/0021-9169(86)90097-8.

Lay, E., Parker, P.A., Light, M., et al., 2018. Midlatitude ionospheric irregularity spectral density as determined by ground-based GPS receiver networks. J. Space Weather Space Clim. 123, 5055–5067. https://doi.org/10.1029/2018JA025364.

Linty, N., Minetto, A., Dovis, F., et al., 2018. Effects of phase scintillation on the GNSS positioning error during the September 2017 storm at Svalbard. Space Weather 16, 1317–1329. https://doi.org/10.1029/2018SW001940.

Liu, Y., Zhou, C., Xu, T., et al., 2021. Review of ionospheric irregularities and ionospheric electrodynamic coupling in the middle latitude region. Earth Planet. Sci. 5, 462–482. https://doi.org/10.26464/epp2021025.

MacDougall, J., Eadie, D.C., 2005. The shape of midlatitude scintillation irregularities. J. Atm. Solar-Terr. Phys. 67, 931–935. https://doi.org/10.1016/j.jastp.2005.02.007.

Mevius, M., van der Tol, S., Pandey, V.N., et al., 2016. Probing ionospheric structures using the LOFAR radio telescope. Radio Sci. 51, 927–941. https://doi.org/10.1002/2016RS006028.

Mikkelsen, I.S., Aarons, J., Martin, E., 1978. Geometrical considerations of 136 MHz amplitude scintillation in the auroral oval. J. Atm. Terr. Phys. 40, 479–483. https://doi.org/10.1016/0021-9169(78)90181-2.

Mohanty, S., Singh, G., Carrano, C.S., et al., 2018. Ionospheric scintillation observation using space-borne synthetic aperture radar data. Radio Sci. 53, 1187–1202. https://doi.org/10.1029/2017RS006424.

Moorcroft, D.R., Arima, K.S., 1972. The shape of the F-region irregularities which produce satellite scintillations – Evidence for axial asymmetry. J. Atm. Terr. Phys. 34, 437–450. https://doi.org/10.1016/0021-9169(72)90045-1.

Phelps, A.D.R., Sagalyn, R.C., 1976. Plasma density irregularities in the high-latitude top side ionosphere. J. Geophys. Res. 81, 515–523. https://doi.org/10.1029/JA081i004p00515.

Portillo, A., Herraiz, M., Radicella, S.M., et al., 2008. Equatorial plasma bubbles studied using African slant total electron content observations. J. Atm. Solar-Terr. Phys. 70, 907–917. https://doi.org/10.1016/j.jastp.2007.05.019.

Prikryl, P., Ghoddousi-Fard, R., Weygand, J.M., et al., 2016. GPS phase scintillation at high latitudes during the geomagnetic storm of 17–18 March 2015. J. Geophys. Res. 121, 10448–10465. https://doi.org/10.1002/2016JA023171.

Priyadarshi, S., Wernik, A.W., 2013. Variation of the ionospheric scintillation index with elevation angle of the transmitter. Acta Geophys. 61, 1279–1288. https://doi.org/10.2478/s11600-013-0123-3.

Prudnikov, A.B., Brychkov, Y.A., Marichev, O.I., 1992. Integrals and Series, vol. 1. CRC Press, Boca Raton.

Rino, C.L., 1979a. A power law phase screen model for ionospheric scintillation: 1. Weak scatter. Radio Sci. 14, 1135–1145. https://doi.org/10.1029/RS014i006p01135.

Rino, C.L., 1979b. A power law phase screen model for ionospheric scintillation: 2. Strong scatter. Radio Sci. 14, 1147–1155. https://doi.org/10.1029/RS014i006p01147.

Rino, C.L., 2011. The Theory of Scintillation with Applications in Remote Sensing. Wiley, New Jersey.

Rino, C.L., Fremouw, E.J., 1977. The angle dependence of singly scattered wavefields. J. Atm. Terr. Phys. 39, 859–868. https://doi.org/10.1016/0021-9169(77)90166-0.

Rino, C.L., Livingston, R.C., E.Whitney, H., 1976. Some new results on the statistics of radio wave scintillation 1. Empirical evidence for Gaussian statistics. J. Geophys. Res. 81, 2051–2057. https://doi.org/10.1029/JA081i013p02051.

Rino, C.L., Livingston, R.C., Matthews, S.J., 1978. Evidence for sheet-like auroral ionospheric irregularities. Geophys. Res. Lett. 5, 1039–1042. https://doi.org/10.1029/GL005i012p01039.

Rino, C.L., Livingston, R.C., Tsunoda, R.T., et al., 1983. Recent studies of the structure and morphology of auroral zone F region irregularities. Radio Sci. 18, 1167–1180. https://doi.org/10.1029/RS018i006p01167.

Rino, C.L., Owen, J., 1980. The structure of localized nighttime auroral zone scintillation enhancements. J. Geophys. Res.: Space Phys. 85, 2941–2948. https://doi.org/10.1029/JA085iA06p02941.

Rogers, N.C., Quegan, S., Kim, J.S., et al., 2014. Impacts of ionospheric scintillation on the BIOMASS P-band satellite SAR. IEEE Trans. Geosci. Remote Sens. 52, 1856–1868. https://doi.org/10.1109/TGRS.2013.2255880.

Secan, J.A., Bussey, R.M., Fremouw, E.J., et al., 1995. An improved model of equatorial scintillation. Radio Sci. 30, 607–617. https://doi.org/10.1029/94RS03172.

Secan, J.A., Bussey, R.M., Fremouw, E.J., et al., 1997. High-latitude upgrade to the wideband ionospheric scintillation model. Radio Sci. 32, 1567–1574. https://doi.org/10.1029/97RS00453.

Secan, J.A., Fremouw, E.J., 1983. Improvement of the scintillation-irregularity model in WBMOD. Technical Report DNA-TR-81-241 Defence Nuclear Agency, Nowherecity, Washington DC.

Secan, J.A., Fremouw, E.J., Robins, R.E., 1987. A review of recent improvements to the WBMOD ionospheric scintillation model. In: Goodman, J.M., Klobuchar, J.A., Joiner, R.G., Soicher, H. (Eds.),

The Effect of the Ionosphere on Communication, Navigation, and Surveillance Systems. Naval Research Lab, Washington DC, pp. 607–616.

Semmling, A.M., Beckheinrich, J., Wickert, J., et al., 2014. Sea surface topography retrieved from GNSS reflectometryphase data of the GEOHALO flight mission. Geophys. Res. Lett. 41, 954–960. https://doi.org/10.1002/2013GL058725.

Singleton, D.G., 1970. The effect of irregularity shape on radio star and satellite scintillations. J. Atm. Terr. Phys. 32, 315–343. https://doi.org/10.1016/0021-9169(70)90005-X.

Sinno, K., Minakoshi, H., 1983. Experimental results on satellite scintillations due to field-aligned irregularities at mid-latitudes. J. Atm. Terr. Phys. 45, 563–567. https://doi.org/10.1016/S0021-9169(83)80071-3.

Basu, Sunanda, Basu, S., Costa, E., et al., 1991. Interplanetary magnetic field control of drifts and anisotropy of high-latitude irregularities. Radio Sci. 26, 1079–1103. https://doi.org/10.1029/91RS00586.

Tatarski, V.I., 2016. Wave Propagation in a Turbulent Medium. Dover, New York.

Tereshchenko, E.D., Khudukon, B.Z., Kozlova, M.O., et al., 1999. Anisotropy of ionospheric irregularities determined from the amplitude of satellite signals at a single receiver. Ann. Geophys. 17, 508–518. https://doi.org/10.1007/s00585-999-0508-4.

Uscinski, B.J., 1977. The Elements of Wave Propagation in Random Media. McGraw-Hill, New York.

Vasylyev, D., Béniguel, Y., Wilken, V., et al., 2022. Modeling of ionospheric scintillation. J. Space Weather Space Clim. 12, 22. https://doi.org/10.1051/swsc/2022016.

von Karman, T., 1948. Progress in the statistical theory of turbulence. Proc. N.A.S. 34, 530–539. https://doi.org/10.1073/pnas.34.11.530.

Wang, J., Morton, Y.T., 2017. A comparative study of ionospheric irregularity drift velocity derived from a GNSS receiver array and Poker Flat Incoherent Scatter Radar measurements during high-latitude ionospheric scintillation. J. Geophys. Res. 122, 6858–6881. https://doi.org/10.1002/2017JA024015.

Wernik, A.W., Alfonsi, L., Materassi, M., 2007. Scintillation modeling using in situ data. Radio Sci. 42, RS1002. https://doi.org/10.1029/2006RS003512.

Wernik, A.W., Liu, C.H., Yeh, K.C., 1983. Modeling of spaced-receiver scintillation measurements. Radio Sci. 18, 743–764. https://doi.org/10.1029/RS018i005p00743.

Yakovlev, O.I., Matyugov, S.S., Vilkov, I.A., 1995. Attenuation and scintillation of radio waves in the Earth's atmosphere from radio occultation experiments on satellite-to-satellite links. Radio Sci. 30, 591–602. https://doi.org/10.1029/94RS01920.

Yang, Z., Morton, Y.T.J., 2020. Low-latitude GNSS ionospheric scintillation dependence on magnetic field orientation and impacts on positioning. J. Geodesy 94, 59. https://doi.org/10.1007/s00190-020-01391-7.

Yeh, K.C., Liu, C.-H., 1982. Radio wave scintillations in the ionosphere. Proc. IEEE 70, 324–360. https://doi.org/10.1109/PROC.1982.12313.